The Meteoritical Society

Meteoritics & Planetary Science 59, Nr 7, 1577–1609 (2024)
doi: 10.1111/maps.14170

Ries magnetic mineralogy: Exploring impact and post-impact evolution of crater magnetism

Bruno Daniel Leite MENDES[1,*], Agnes KONTNY[1], Katarzyna DUDZISZ[2], and Franziska D. H. WILKE[3]

[1]Institute of Applied Geosciences, Karlsruhe Institute of Technology, Karlsruhe, Germany
[2]Institute of Geophysics, Polish Academy of Sciences, Warsaw, Poland
[3]Helmholtz Centre Potsdam – Deutsches GeoForschungsZentrum GFZ, Telegrafenberg, Potsdam, Germany

***Correspondence**
Bruno Daniel Leite Mendes, Institute of Applied Geosciences, Karlsruhe Institute of Technology, Karlsruhe, Germany.
Email: bruno.mendes@kit.edu

(Received 23 August 2023; revision accepted 28 March 2024)

Abstract–Large-scale impact events are some of the most catastrophic and instantaneous geological processes in nature, and leave in their wake conspicuous geological structures with characteristic magnetic anomalies. Despite magnetic anomalies in craters being well-documented, their relationship with the magnetic mineral composition of the target and impactites is not always straightforward. Furthermore, the influence of impact shock and post-impact events in the magnetism of natural craters remains elusive. In the Ries crater, Germany, the negative magnetic anomalies are attributed to a reverse polarity remanent magnetization in the impact-melt bearing lithologies. We report new chemical, rock-, and mineral-magnetic data from the shocked basement and impactites, from surface samples, NR73 and SUBO-18 boreholes, and explore how temperature and hydrothermalism may influence the magnetic mineralogy in the crater. We identified shocked, pure magnetite in the basement, and low-cation substituted magnetite in the impactites as the main magnetic carriers. The shocked basement is demagnetized but remains largely unaltered by post-impact hydrothermalism, while the impactites show weak magnetization and are extensively altered by neutral-to-reducing post-impact hydrothermalism. We suggest that the magnetic mineralogy of the demagnetized uplifted basement may contribute significantly to the magnetic anomaly variation, in line with recent findings from the Chicxulub peak-ring.

INTRODUCTION

Large-scale impact events are some of the most catastrophic and instantaneous geological processes in nature. Hypervelocity impacts release high amounts of energy and generate pressures that will vaporize, melt, and metamorphose the target rock, and may have large-scale environmental implications such as a contribution to extinction events (e.g., Hildebrand et al., 1991; Schulte et al., 2010). These events leave in their wake large conspicuous impact structures with very characteristic features, such as gravity and magnetic anomalies (Pilkington & Grieve, 1992). These physical anomalies have been used to detect these structures even after millions of years of sedimentary burial.

Magnetic anomalies in impact structures are very well documented phenomena (e.g., Gulick et al., 2008; Hildebrand et al., 1991; Pilkington & Grieve, 1992; Ugalde et al., 2005), but their relationship with the magnetic mineralogy of both shocked target rocks and impact-derived rocks is not always straightforward. Shock-related reduction in the total magnetization (M_t), which is the sum of natural remanent magnetization (NRM) and induced magnetization ($M_t = \mathrm{NRM} + \kappa^* B$, where κ is magnetic susceptibility and B is an ambient magnetic field, in this case Earth's magnetic field) is well

documented in literature. The loss of NRM in target rocks has been studied in detail over the last decades (e.g., Bezaeva et al., 2007, 2010; Gattacceca et al., 2010; Gilder et al., 2006; Jackson et al., 1993; Kletetschka et al., 2004; Louzada et al., 2007, 2011; Pearce & Karson, 1981; Tikoo et al., 2015), demonstrating that even at pressures under 2 GPa, multidomain (MD) magnetite, the most important magnetic mineral in the Earth's crust, may lose up to ~90% of its pre-shock NRM. While shockwave deformation may impart a shock remanent magnetization (SRM, e.g., Fuller, 1977; Gattacceca et al., 2006, 2007; Louzada et al., 2011; Srnka et al., 1979; Tikoo et al., 2015), this is often a very inefficient process, and creates a weak magnetization (only few percent of the original NRM).

Research into the loss of magnetic susceptibility (κ) in experimentally shocked magnetite is more recent and has shown that even relatively low shock pressures of 5 GPa cause a reduction of up to 90% in pure magnetite (Reznik et al., 2016). The reduction in κ is related to physical processes, such as grain fracturing, fragmentation, and intra-crystalline lattice defects, that lead to an apparent decrease in the domain state of originally MD magnetite. Lattice defects enhance domain wall pinning (e.g., Lindquist et al., 2015), and together with fracturing, cause a reduction in the apparent magnetic grain size, increase in magnetite coercivity, and further reduction in κ (Reznik et al., 2016). However, follow-up studies on the same shocked magnetite samples have found that through the exposure of shocked magnetite to high temperatures (up to 700°C), thermal annealing of the crystal lattice defects could restore some of the lost magnetic properties and κ, and reduce wall pinning effects, leading to a decrease in coercivity and an apparent increase in domain state (Kontny et al., 2018; Mendes & Kontny, 2024). The shock-derived reduction in both remanent and induced (through reduction of κ) magnetization in shocked target rocks, and the potential post-impact restoration of some of these properties, will invariably contribute to the magnetic anomaly pattern in impact structures.

However, the effects of impact shock and temperature-related post-impact restoration of magnetic properties, and the influence that these phenomena have in natural impact craters, remain largely unexplored. A recent study in the ~200-km-diameter Chicxulub impact crater (first discovered by Penfield & Camargo, 1981) has found that the prominent negative magnetic anomaly in the peak-ring is controlled by the shock-induced demagnetization ($\sim 0.01\ A\ m^{-1}$) and reduction of κ ($\sim 50 \times 10^{-5}$SI) in the uplifted shocked granitoid basement (Mendes et al., 2023). Here, large magnetite grains (>500 μm) show around ~90% lower κ than intact (not shocked) granite containing similar amounts of magnetite ($\kappa = \sim 1000 \times 10^{-5}$SI, see e.g., Ishihara, 1979; Ishihara et al., 2000, and discussion in Mendes et al., 2023). A post-impact, long-lasting (up to 2 Myr) hydrothermal system with temperatures up to 450°C (Kring et al., 2020) was not enough to anneal the internal defects and restore some of κ (Mendes et al., 2023), or significantly imprint a secondary NRM in the basement (Mendes et al., 2023). Furthermore, the suevite (impact breccia) in Chicxulub is magnetically very weak (Mendes et al., 2023), and show very low amounts of magnetite, mostly concentrated in small basement or melt fragments.

These observations in the Chicxulub suevite contrasts with the extensively studied ~26 km diameter Nördlinger Ries impact crater (referred to as "Ries crater" henceforth), in Germany. Here, the magnetization is carried by magnetite, newly formed in the impact melt of the suevite, at the time of deposition at high temperatures (up to 900°C in the suevite and >2000°C for the impact melt, Osinski et al., 2004). It was suggested that a very strong reverse polarity NRM in the suevite is the reason for the intense negative anomalies in the inner basin of the crater (Arp et al., 2019; Iseri et al., 1989; Pohl, 1965; Pohl et al., 1977, 2010; Pohl & Angenheister, 1969). Despite the extensive amount of research, the magnetic characteristics and contribution of the shocked basement have not yet been constrained. Furthermore, the contiguous layers of impact melt in the Ries crater ubiquitously shows low NRM and κ, the reason for which is also unclear. Post-impact hydrothermalism is also reported in this crater (Arp et al., 2013; Naumov, 2005; Osinski et al., 2004, 2013; Sapers et al., 2017), although with lower temperatures than in Chicxulub (max. 300° in the inner crater, 130°C in the outer regions, see Osinski, 2005) and with a shorter lifespan (max. 250 kyr, Arp et al., 2013). The influence that hydrothermalism had in the magnetic mineralogy and particularly in their magnetic properties also remains unexplored.

The aim of this study was to fill these knowledge gaps in the magnetic mineralogy of the Ries crater lithologies, with special focus on the magnetic properties of the shocked magnetite in the basement. We also constrained the influence of post-impact exposure to natural high temperatures in the basement due to the impactites, and studied the influence of hydrothermal alteration on crater magnetism. We investigated drill cores from FBN73 and SUBO-18 (NR73 and SUBO henceforth), and collected surface samples from the megablock zone at four locations (Polsingen, Aumühle, Altenbürg, and Wengenhausen). Through rock-magnetic, microscopical, and mineral chemical methods, we discriminated pre-, syn-, and post-impact geological processes, to gain insight into the different contributions to the magnetic anomaly. Based on our data and previous literature, we propose a conceptual model of the evolution of the magnetic phases

before, during, and after the impact. Finally, we present a short comparison between the Chicxulub and Ries crater system.

GEOLOGICAL SETTING AND SAMPLES

Crater Structure and Stratigraphy

The ~26-km-diameter Ries impact crater is located in southern Germany (Figure 1a). It was formed in a sequence of layered Permian, Mesozoic, and Oligocene/Upper Miocene sediments of ~600 m thickness, overlaying crystalline basement composed of Variscan granite, gneiss, and amphibolite (Figure 1b,c; e.g., Graup, 1975). The age of the impact is dated to 14.808 ± 0.038 Ma (Schmieder et al., 2018). This crater is classified as a complex impact structure (e.g., Pohl et al., 1977), and is divided into an inner crater, delimited by the "inner ring" with ~12 km in diameter, and an outer megablock zone (Figure 1b). The inner crater is characterized by shocked Variscan basement overlain by an allochthonous crater-fill deposit, called crater suevite (see e.g., Osinski et al., 2004), later covered by Tertiary crater-fill lake sediments (Figures 1b,c and 2).

The inner ring consists of uplifted shocked basement and separates the inner crater from the megablock zone. The inner ring is also the boundary of the post-impact crater lake fill (Figure 1c). The term "megablock" refers to "displaced fragments of all stratigraphic units of the target rocks, which are larger than 25 m in size and can be geologically mapped" (Pohl et al., 1977). The megablocks are covered by the Bunte Breccia, an impact breccia derived predominantly from the Mesozoic sedimentary target (e.g., Fraas & Branco, 1901; Hüttner et al., 1969; Hörz et al., 1983). This is a poorly sorted, glass-free breccia which comprises the most volumetrically abundant proximal ejecta, interpreted as a continuous ejecta blanket (e.g., Morrison & Oberbeck, 1978; Oberbeck, 1975). Two drill cores were sampled for this study, one in the inner crater (NR73), and one on the inner flank of the inner ring (SUBO) (Figures 1c and 2).

The most characteristic rock type of the Ries crater is suevite (Schwabenstein), described here for the first time (Sauer, 1920). Currently, suevite is defined as a polymict breccia with a particulate matrix, containing lithic and mineral clasts at all stages of shock metamorphism, including impact melt particles. The suevite is described to consistently overlie the Bunte Breccia (Figure 1b,c), and a distinction is made in literature between "main" and "basal" suevite (Bringemeier, 1994). The main suevite is unsorted and well consolidated, with abundant impact glass clasts, and a preferred horizontal orientation of flat glass clasts. This type is the most abundant, and we sampled it at Altenbürg and Wengenhausen, in the megablock zone (Figure 1b). In contrast, the basal suevite is fine grained and poorly consolidated, moderately to well sorted, and deficient in glass clasts (e.g., Chao, 1978), which we sampled at the Aumühle quarry.

Coherent impact melt rock or "red suevite" is rare in the Ries crater compared with other craters (e.g., Chicxulub). The question of "missing melt" in the Ries crater has been raised before (e.g., Graup, 1999; Grieve, 1999; Osinski, 2003, 2004; Osinski et al., 2004, 2008; Pohl et al., 2010; Wünnemann et al., 2008); however, no concrete explanations have been provided so far. It occurs as isolated bodies with lateral extents of up to 50 m (Pohl et al., 1977), and is found on the surface overlaying the Bunte Breccia, containing variably shocked basement (predominantly granite) and mineral clasts (predominantly quartz) (Engelhardt & Bertsch, 1969, Pohl et al., 1977). Alkali feldspar, plagioclase, quartz, and ilmenite comprise the microcrystalline groundmass (Osinski, 2004). This "red suevite" is sampled in Polsingen, and in parts of the borehole SUBO (Figure 2).

Lithology of the Drill Cores

NR73

The scientific drilling project Nördlingen 73 was drilled in 1973 at about 3.5 km from the crater center in a region of negative magnetic anomaly (Figure 1d). The borehole is 1206 m deep, and the core is the only one reaching the shocked crystalline basement at depth. It also comprises the longest continuous core of suevite in the crater (~200 m, Figure 2). The lithologies of interest are found below 314 m of post-impact sedimentary fill, and can generally be subdivided into three sections (e.g., Meyer, 2012).

Graded suevite (314–331 m) is interpreted as subaerial fallback material from the ejecta plume (Jankowski, 1977). This section shows a transition from medium-grained gravel at its base to silt at its top and is intercalated by pervasively altered breccias. The melt clasts in this subunit are weathered, but this weathering decreases with depth (Meyer, 2012).

Melt-rich suevite (331–520 m) refers to a section of suevite with an increased melt-clast content. Between 331 and 390 m, the lithic and melt contents remain constant with a slight increase in grain size. From 390 m, large basement blocks intersect the suevite (e.g., Bauberger & Mielke, 1974), and below 436 m the impact melt contents decrease until no melt can be discerned macroscopically in the suevite.

Shocked basement (520–1206 m) refers to a sequence of Variscan basement (Graup, 1975) which has been shocked during the impact. An irregular sequence of gneiss, amphibolite, and granite dominates between 520

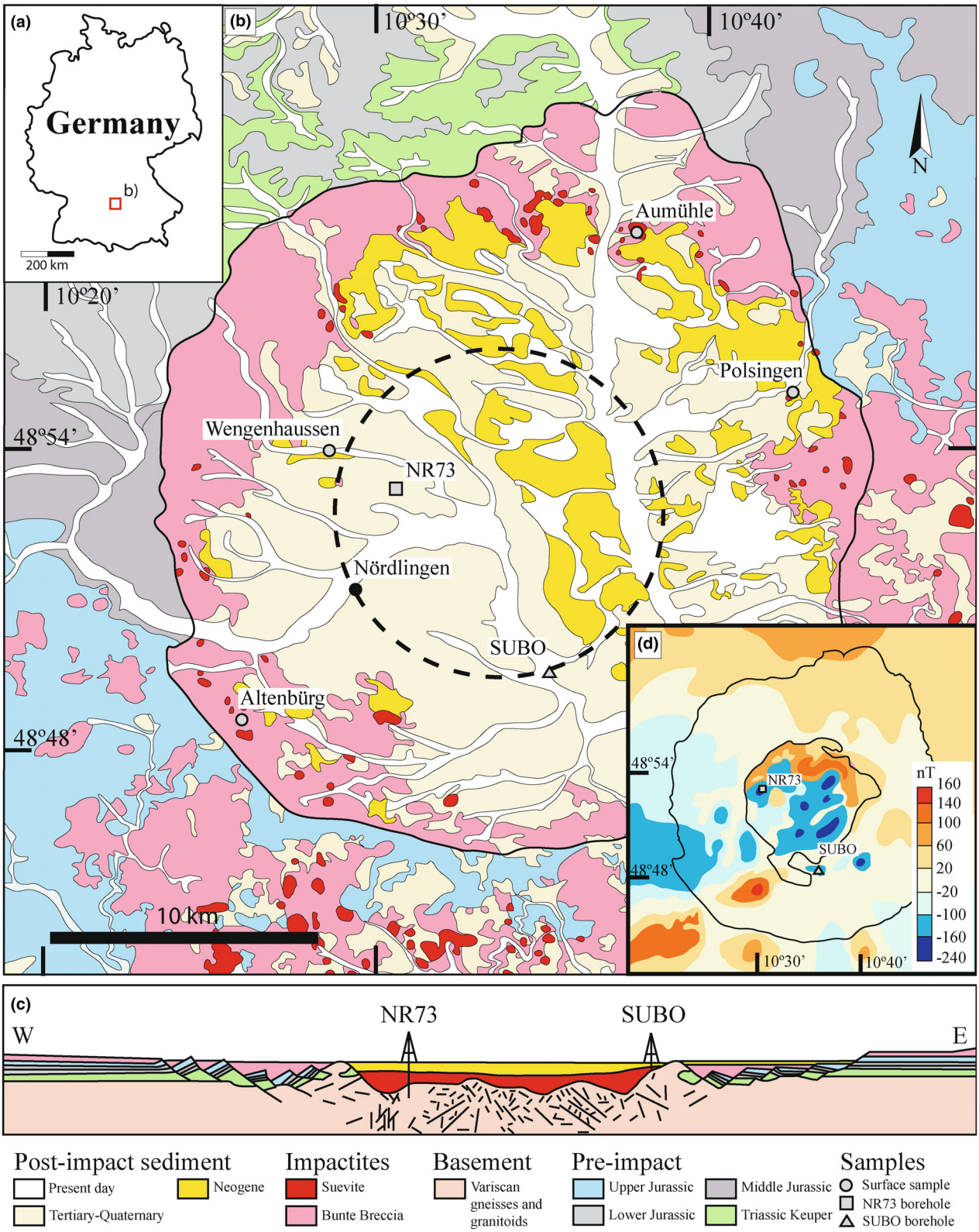

FIGURE 1. (a) Geographic location of the Nördlinger Ries impact crater in Germany; (b) lithological map of the Ries crater and sampling locations (modified after Zhao et al., 2022); (c) sketch of the crater profile (modified after Zhao et al., 2022); and (d) aeromagnetic anomaly map (nT; after Pohl et al., 2010). (Color figure can be viewed at wileyonlinelibrary.com)

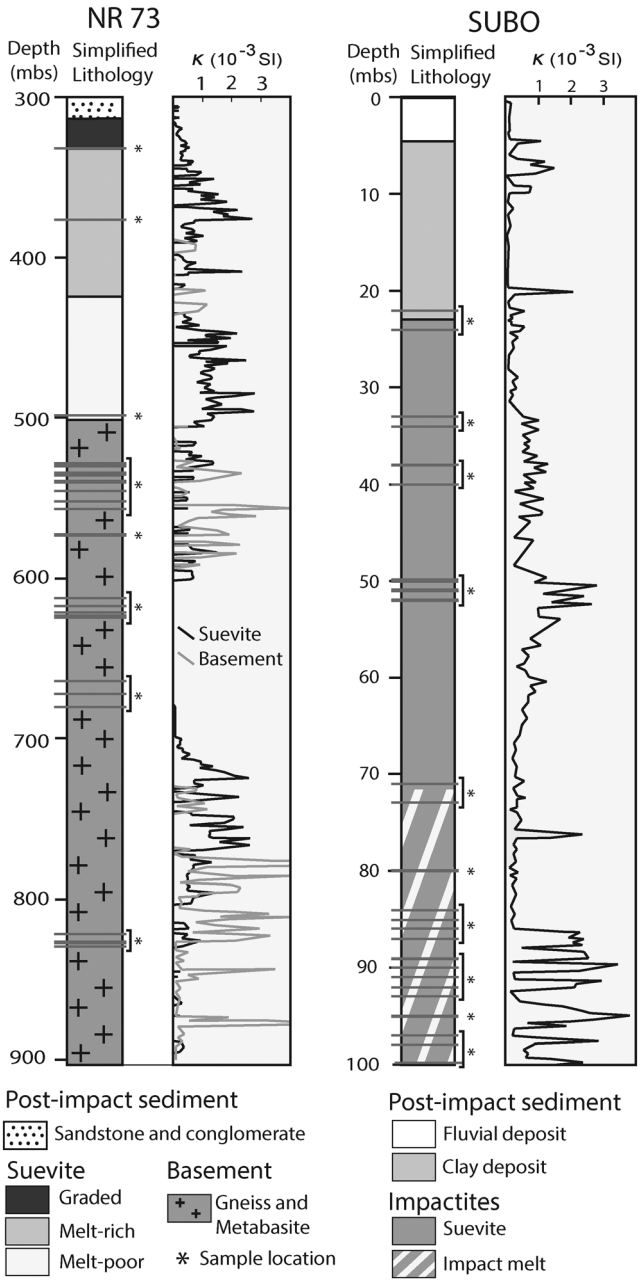

FIGURE 2. Simplified lithological units of boreholes NR73 and SUBO, with highlighted sample locations and downhole magnetic susceptibility (κ) data. NR73 lithology and κ modified after Pohl (1977); SUBO lithology and κ modified after Pohl et al. (2010).

and 820 m, below which metabasites are predominant. We focused our sampling on the gneiss–amphibolite–granite sequence, where primary shocked magnetite grains are expected. We used available, low-resolution downhole magnetic susceptibility and NRM intensity data from literature (Figure 2; after Pohl, 1977) to select sampling intervals, attempting to sample regions at the stronger end of intensities of NRM and κ. The basement rocks are mostly continuous, disrupted locally by intercalations or dykes of melt-poor suevite, where melt particles are not macroscopically detectable. This suevite shows also a decreased grain size with depth. Some of these dikes have been interpreted as lateral intrusions by highly turbulent flow, during the crater forming processes (e.g., Stöffler, 1977; Stöffler & Grieve, 2007).

SUBO

SUBO was drilled in 2006 in the southern section of the inner ring at Enkingen, into a local negative magnetic anomaly (Pohl et al., 2010, Figures 1d and 2). It has a total depth of ~100 m and consists of ~21 m of crater-fill sediments (not considered in this study), and of 79 m of suevite and impact melt rock (Figure 2, Pohl et al., 2010). The impact rock is a complex sequence of multiple brecciated suevite-melt lithologies, which we broadly subdivide into "suevite" (21.19–40 m), "clast-and-melt rich suevite" (41–58 m), and "impact melt" (58–99.98 m) units, after the dominant macroscopic characteristics described in Pohl et al. (2010).

Suevite (21.19–40 m) is characterized by a sandy–clayey matrix, without a carbonate component (Pohl et al., 2010). Here, the suevite is generally coherent, with varied amounts of melt clasts, and evidence of secondary carbonate impregnation (Pohl et al., 2010). Melt fragments show a preferred subhorizontal orientation, and lithic clasts are abundant, mostly comprising felsic gneiss and granitoid basement (Pohl et al., 2010). The suevite unit also shows strong hydrothermal alteration, with the groundmass substantially altered to phyllosilicates, mainly illite and smectite as alteration products, and rare chlorite, together with both primary and secondary Fe-sulfides, mainly pyrite (Sapers et al., 2017).

Clast- and melt-rich suevite (41–71 m) is friable and highly altered, with little core recovery. In this section, we sampled only a 3-m-long section where the quality was suitable and coherent whitish-pink suevite matrix contained increased impact melt and lithic clasts. From 58 to 71 m, no cores were recovered.

Melt-rich suevite (71–99.98 m) is dominated by melt-clasts. A characteristic dark-red color in the melt suggests the presence of hematite. Melt clasts form up to 80% of the rock, but individual melt bodies within the previously described white-pink groundmass can be found down to a depth of 86.24 m, locally intersected by suevite. From 86.24 to 99.98 m, the remaining rock is a coherent and continuous section of impact melt rock.

Pohl et al. (2010) describes a pseudo-single domain (PSD) magnetite as the main ferrimagnetic mineral in SUBO, with sulfidic ferrimagnetic minerals such as pyrrhotite not described. In the crystalline basement clasts, magnetite is suggested to be primary but secondary

magnetite also occurs, produced by impact-induced thermal decomposition of mafic minerals. Hematite also is found in some samples. Magnetic modeling suggests that the granitic basement of the inner ring is located between 10 and 20 m below the bottom of the drill core (Pohl et al., 2010).

Hydrothermalism

Post-impact hydrothermal activity is a common feature in impact craters with impact melt-bearing lithologies and an elevated geothermal gradient in central uplifts being the main source of heat (e.g., Ames et al., 1998; Hode et al., 2004; Phukon et al., 2024; Naumov, 2005; Newsom, 1980; Osinski et al., 2013). The hydrothermal alteration in the Ries crater is spatially extensive but not laterally continuous (Sapers et al., 2017). Pervasive and high-temperature alteration is restricted to the inner crater, where NR73 and SUBO were drilled. Ejecta in the megablock zone shows locally intense lower temperature hydrothermal alteration (Sapers et al., 2017).

As hydrothermal alteration is localized and concentrated within the suevite, their deposition at temperatures >750–900°C (Osinski et al., 2013) is suggested as dominant heat source. The initial melt temperature of the impact melt was also quite high (>2000°C) with relatively high water content (>5 wt%) (Osinski et al., 2004), whose latent heat might also have played a role. Hydrothermal activity lasted up to ~250,000 years after the impact (Arp et al., 2013). A two-stage cooling is proposed in literature (e.g., Naumov, 2005; Sapers et al., 2017), with a first stage involving rapid convection-driven cooling above boiling temperatures (about 200–300°C, Osinski, 2005) through steam generation and degassing, and a second stage with a long-lasting gradual cooling. The fluid sources are described to vary locally, but a combined contribution from both shallow and deep sources is likely, due to fluid–rock interaction with the different target lithologies. In the megablock zone meteoric water dominates, while in the inner crater the fluids derive from the crater lake and the high fracturing and disruption of the groundwater table (Sapers et al., 2017). The heterogeneity of the fracture patterns will further contribute to the different alteration intensities found throughout the crater.

The most pervasive alteration is found in the inner crater, where the crater lake allowed for saturated conditions of the fluids (Osinski, 2005; Sapers et al., 2017). The high-temperature early stage is restricted to the crater suevite and is characterized by K-metasomatism throughout the upper sections (Osinski, 2005). Basement alteration is limited to minor albitization and chloritization, which also occurs in this early stage (Osinski, 2005). In the suevite, the main stage of alteration is characterized by a complete replacement of all impact glass and basement clasts, forming saponite, montmorillonite, and analcite (Osinski, 2005). Alkali and calcic zeolites are predominant in the altered suevite, indicating weakly alkaline hydrothermal solutions. These alkaline fluids are further responsible for the deposition of goethite throughout the drill core NR73 as minor phase (Osinski, 2005).

To date, the hydrothermal alteration of core SUBO has not been investigated in detail. However, its location in the inner ring, the observation of crater-lake sediments, and crater suevite suggest that the hydrothermal system affecting SUBO is comparable to that of NR73. It is unclear at which stage the formation of hematite in impact melt rocks and red suevite of SUBO occurred, as it can represent either a low-temperature hydrothermal phase or vapor deposition, or a combination of the two, similar to the surface melts in Polsingen (Osinski, 2004, 2005).

Alteration of surface suevite, including the Aumühle quarry (Sapers et al., 2017), is characterized by the formation of montmorillonite and Ba-phillipsite. The main alteration in this suevite is constrained to be below 100–130°C (Osinski, 2005) and have a slightly more acidic composition in contrast with the inner ring fluids (Muttik et al., 2011; Sapers et al., 2017).

Rock Magnetism

Previous research has been conducted on the characteristic magnetic anomaly patterns in the crater (Pohl, 1965; Pohl et al., 1977, 2010). Spots of negative magnetic intensities are mostly concentrated in the inner ring (Figure 1d) and the surface suevite in the western section of the megablock zone. Previous studies (Arp et al., 2019; Pohl, 1965; Pohl et al., 1977, 2010; Pohl & Angenheister, 1969) have investigated surface samples and drill cores from Otting, Wörnitzostheim, NR73, SUBO, and Erbisberg, and related the intense negative magnetic anomalies to a generally reverse polarity of NRM in the high-temperature suevites. In surface samples, paleomagnetic directions with Dec/Inc = ~194°/−57° (Pohl & Angenheister, 1969) and Dec/Inc = 188.6°/−60.8° (α_{95} = 0.78°; Iseri et al., 1989) are described. These directions are consistent with an acquisition of magnetization at the time of impact. The studies further suggest that titanomagnetite with low Ti concentration is the main carrier of magnetization in the Ries suevite. Maghemite formed during low-temperature oxidation of titanomagnetite is also described, which records the same direction as the titanomagnetite, indicating a hydrothermal alteration shortly after the emplacement of the suevite (Iseri et al., 1989).

Surface Samples

Altenbürg shows the highest intensities of NRM (0.4 A m^{-1}), followed by Polsingen (0.2 A m^{-1}), and being the weakest at Aumühle (<0.1 A m^{-1}; Pohl et al., 2010). The aim for resampling these surface samples was a discrimination between pre- and syn-impact magnetite formation, which may help to better understand the magnetic evolution and anomaly pattern distribution. Samples from the Wengenhausen location have never been studied before. Finally, the sampling of the Polsingen melt rocks allows us a comparison with the melt sections of SUBO.

NR73

Previous data from NR73 have been published by Pohl et al. (1977) and Pohl (1977; Figure 2). These data show a consistent reverse inclination ~−60° and high average NRM intensity in the suevite (~2.7 A m^{-1}), despite a wide variation along the core. High intensity was only found in the suevite, while the shocked basement shows a scatter of positive and negative inclinations, with very low NRM intensities, and decreased magnetic susceptibility in the gneisses and granitoids, and higher values in metabasite sections at greater depths (Figure 2, Pohl, 1977). To our knowledge, no investigations of the magnetic mineralogy and properties of the shocked basement has been done until now, aside from the low-resolution downhole κ and NRM intensity data published by Pohl (1977; Figure 2).

SUBO

A detailed magnetic survey including rock magnetic investigations was performed by Pohl et al. (2010) in the SUBO drill cores. This study confirmed again a stable reversed polarity magnetization in suevite, in a local negative magnetic anomaly (Figure 1d). The inclination in the "melt" unit of the SUBO drill core shows the same ~−60° average inclination, but the reported intensity (1.5 A m^{-1}) is lower than that described from the NR73 drill cores. Magnetic susceptibility seems to be generally lower in the suevite (~0.5×10^{-3} SI), than in the impact melt rock (up to 8×10^{-3} SI), but conversely the melt has lower NRM intensities than the suevite. This leads to very high Koenigsberger (Q-) ratios in the suevite (10–40), whereas in the melt, Q-ratios are generally lower (~5), but still showing a clear dominance of remanence over induced magnetization ($Q > 1$).

METHODS

Material

Seventy-two samples were used for this study, including four surface samples collected in the megablock zone (Figure 1b), 32 samples from the drill core NR73 (Figure 2, left), and 36 samples from the drill core SUBO (Figure 2, right). All the drill core samples were numbered according to their depth (Figure 2).

Samples from NR73 comprise the shocked Variscan basement (25 samples) and suevite (seven samples, three of which are intercalated with the basement blocks). Samples from SUBO comprise seven suevite samples, nine basement-melt intercalated samples, and 20 impact melt samples. All four surface samples comprise impact-melt rich suevite.

We provide all data files used for this study in Supplemental files. File S1 is a text file with a short overview of the contents of the remaining supplemental files. A list with sample names, depths, and lithology can be found in File S2.

Microscopic and Mineral Chemical Analysis

We performed transmitted and reflected light microscopy at the Karlsruhe Institute of Technology (KIT) using a Leitz polarizing microscope. For some samples, we applied oil-based ferrofluid coatings (FerroTec EMG 508 and EMG 905) for easier visualization of the ferromagnetic phases. A total of 189 electron probe microanalysis (EPMA) spot-measurements and backscattered electron (BSE) images were taken of 11 representative carbon-coated samples from the suevite surface samples (three samples), NR73 (five samples), and SUBO (three samples) at the Deutsches GeoForschungsZentrum (GFZ) in Potsdam, Germany. We used a JEOL Hyperbole JXA-8530F PLUS microprobe, with five wavelength dispersive spectrometers (WDSs) for quantitative analyses and an energy dispersive X-ray (EDX) detector for overview phase identification. For quantitative measurements, we applied 15 kV, 100 nA, and a surface probe size of 2 µm. We used natural and synthetic standards for the calibration of Cr, Mg, Fe, O, Al, Ti, and Mn such as ASTIMEX© magnetite for Fe and O. This routine allowed us to measure individual element weight percentage (wt%), with oxygen measured individually, rather than oxide wt%. To obtain the spinel formula, we have performed two calculations, one assuming four oxygen molecules, and another assuming three cations, for stoichiometry control calculation. We present our results in the text assuming four oxygen atoms for easier readability. Further, we calculated the average amount of vacancies in the magnetite measurements according to: vacancies = 3−[sum of cations], for the formulas normalized to four oxygen atoms. Samples were checked randomly for further accessory elements using EDX, but no other elements appeared in quantities larger than the detection limits (≤100 ppm (1 s)). Vacancies are therefore likely and well explainable by geochemical processes.

Rock Magnetic Methods

We performed temperature-dependent magnetic susceptibility measurements (κ–T), bulk-magnetization, and bulk magnetic susceptibility measurements, as well as isothermal remanent magnetization (IRM) component and hysteresis loop analysis, to investigate the magnetic properties of our samples.

κ–T curves and bulk κ measurements were performed at the KIT using an AGICO (Brno, Czech Republic) KLY-4S Kappabridge, at an applied field of 300 A m^{-1} and a frequency of 970 Hz. For κ–T experiments, we used a CS-L and CS-3 unit for the instrument, which allows us to make low-temperature and high-temperature measurements. Low-temperature "LT" measurements were performed by applying liquid nitrogen to the CS-L cryostat and cooling the sample down to ~−192°C and measuring κ throughout warming in contact with ambient atmosphere, which causes warming rates to be faster at the beginning of the experiment. High-temperature "HT" measurements were performed by heating the CS-3 furnace from room temperature (RT) up to 700°C, and cooling it to 40°C, at a constant rate of 12°C min^{-1}. High-temperature measurements were performed in a flowing argon atmosphere (133 mL min^{-1}, Ar purity of 99.998%) to minimize oxidation. During the experiment, temperature is measured with a Pt resistance thermometer in contact with the samples. The accuracy of these thermometers is ±1°C up to 150°C, and ±3°C from 150°C up to 700°C (Lattard et al., 2006). Bulk κ measurements were also performed using the KLY-4S Kappabridge, with an applied field of 300 A m^{-1} for all samples. Bulk κ is determined by averaging three measurements per sample, and applying holder corrections to this average value.

NRM intensities were measured manually using an AGICO JR-5/5A Spinner Magnetometer at KIT. When samples did not have the standard cylindrical shape, cylindrical holders were used to maintain the material stable during measurement. The values were determined by averaging three measurements per sample, and applying mass and holder corrections after measuring.

Hysteresis loops were measured in order to investigate the content of magnetic particles, the mineralogy and magnetic grain size. A Day diagram (Day et al., 1977) with SD-MD mixing lines (Dunlop, 2002) was prepared using the hysteresis parameters obtained from these loops. Our measurements were performed at the Institute of Geophysics of the Polish Academy of Sciences, in Warsaw, Poland, using an alternating gradient magnetometer (MicroMag AGM 2900, Princeton Measurement Corporation, USA) with a maximum operating field of 1 T. We determined the hysteresis parameters coercivity (B_c), saturation magnetization (M_s) and remanent magnetization (M_{rs}) after applying paramagnetic contribution (high-field linear trend) correction, background signal correction, and mass normalization. The coercivity of remanence (B_{cr}) was estimated from direct current back-field demagnetization (DCD) of IRM.

DCD curves are also used for IRM modeling, and were measured in the same instrument. Cumulative log-Gaussian functions were applied for a statistical analysis of the curves according to Kruiver et al. (2001). Three parameters describe the magnetic components: saturation IRM (SIRM), which is proportional to the magnetic mineral content in the sample; the mean coercivity of remanence of the grain population that constitutes each component, at which half of the SIRM is reached ($B_{1/2}$), and dispersion parameter (DP), which corresponds to the individual cumulative log-normal distribution. We focus our discussion on the mean coercivity of remanence in the text for easier readability.

Magnetic Transition Temperatures and Susceptibility Parameters

We determined the magnetic transition temperatures from the measured κ–T curves applying the first derivate method for data where the transitions are well defined. In samples where this method is unreliable, we have used the tangent method described by Lied et al. (2020).

The Verwey transition temperature (T_v) was determined in samples where magnetite is present, using the LT curves before (T_v1) and after (T_v2) heating. The Verwey transition for pure stoichiometric magnetite is −153°C (120 K, Verwey, 1939), and is very sensitive to physical (e.g., shock-induced lattice defects or internal crystal stresses, Biaøo et al., 2019; Carporzen & Gilder, 2010; Reznik et al., 2016) and chemical (e.g., cation substitution or vacancies, Aragón et al., 1985; Biaøo et al., 2019) alteration of magnetite.

We identified Curie temperatures from the HT curves during heating (T_c1) and cooling (T_c2). This temperature characterizes the transition from ferro- to paramagnetic behavior in all magnetic minerals, and allows for a quick identification of the magnetic carriers. Pure magnetite has a characteristic sharp drop of κ at a temperature of 578°C, and deviations from this may indicate cation substitution (e.g., Engelmann, 2008; Lattard et al., 2006), or oxidation. The oxidation of non-substituted magnetite forms the oxidized endmember maghemite (γ-Fe_2O_3), with a T_c up to 640°C (e.g., Nishitani & Kono, 1981; O'Reilly, 1984; Özdemir & Dunlop, 2010).

Both LT and HT measurements were normalized to the κ values at RT, and were used to determine three other parameters.

We used *Verwey* and *Hopkinson* peak ratios (T_vPR and HPR, respectively) as proxy for magnetic domain states and their variation throughout heating. A decrease in these ratios after heating is associated with a change in magnetic behavior, consistent with an increase (real or apparent) in domain state, if chemical reactions can be excluded (Dunlop, 2014; Kontny et al., 2018; Mendes & Kontny, 2024). $T_v\text{PR} = \kappa_{max}/\kappa_{15}$, where κ_{15} is the κ value at 15°C and κ_{max} is the maximum value around the Verwey transition (Kontny et al., 2018); $\text{HPR} = \kappa_{max}/\kappa_{40}$, where κ_{40} is κ value at 40°C and k_{max} the maximum value before the Curie temperature (Dunlop, 2014).

The alteration parameter A40[%] characterizes the alteration occurring during the κ–T experiment, as a percentage increase or decrease in κ before and after heating to 700°C. A positive A40 value indicates a post-heating increase in κ, which may suggest the formation of a new ferromagnetic phase during heating (e.g., magnetite from hematite, Mendes & Kontny, 2024; Mendes et al., 2023), or the relaxation of internal crystal lattice strain through thermal annealing (Kontny et al., 2018). A negative A40 indicates a decrease in κ during experiment, which may indicate syn-heating transformation to a mineral phase with lower κ (e.g., maghemite to hematite or titanomaghemite to ilmenite and magnetite).

Finally, the Koenigsberger (Q-) ratio, calculated as $Q = \text{NRM}/(\kappa^* B)$, discriminates the relative importance of remanent ($Q > 1$) or induced magnetization ($Q < 1$) in the total magnetization of a given sample. Total magnetization (M_t) is given by:

$$M_t = \text{NRM} + (\kappa^* B),$$

where NRM is the intensity of the natural remanence magnetization and $\kappa^* B$ is the induced magnetization (B is the present day's Earth magnetic field).

RESULTS

Rock Magnetic Data

Surface Samples

All suevite surface samples ($n = 4$) show Q-ratios above 1 (Figure 3a), ranging from 1.8 to 4.15, despite low NRM intensities (ranging from 2.6×10^{-4} to 37×10^{-4} A m^{-1}, Figure 3b), and low κ (from 3.7×10^{-6} to 33.8×10^{-6} SI, Figure 3a,b). Total magnetizations are quite low, ranging from 3.86×10^{-4} to 47.8×10^{-4} A m^{-1}, with the highest values in the Polsingen melt sample (Table 1).

NR73

The suevite samples ($n = 19$) show a clear dominance of remanent magnetization ($Q > 1$, Figure 3a) with generally high κ (from 2000×10^{-6} to $12{,}000 \times 10^{-6}$ SI, Figure 3b) and NRM (0.2–3 A m^{-1}, Figure 3b). The total magnetization of the suevite is also quite strong, ranging from 2.16×10^{-2} in the suevite dykes in the basement to 3.2 A m^{-1} in the upper suevite section, where it averages 2 A m^{-1} (Table 1) in agreement with earlier reports by Pohl (1977).

In the basement ($n = 29$), the induced magnetization is dominant ($Q < 1$, Figure 3c), although generally low κ (ranging from 4.8×10^{-6} to 3500×10^{-6} SI, Figure 3d) dominate, except for three outlier gneiss samples that locally show higher κ ($23{,}700 \times 10^{-6}$ up to $39{,}100 \times 10^{-6}$ SI). NRM intensity in the basement is also lower than in the suevites (2.9×10^{-4} to 520×10^{-4} A m^{-1}), with the exception of the same three outlier gneiss samples (NRM between 0.5 and 0.9 A m^{-1}; Figure 3d). Despite the lithological differences and the outliers, NRM and κ show a positive correlation (Figure 3d). Total magnetizations are quite low in the basement, ranging from 5.44×10^{-4} to 0.9 A m^{-1}, averaging at 0.1 A m^{-1}, with the exception of the abovementioned gneiss outliers, which range from 1.3 to 2.2 A m^{-1} (Table 1).

SUBO

All SUBO samples show a dominance of NRM over induced magnetization ($Q > 1$), with the exception of one melt outlier (Figure 3a,e). The suevite samples ($n = 6$) show low κ (from 4.2×10^{-6} to 45×10^{-6} SI) and low NRM intensities (4.5×10^{-4} to 70×10^{-4} A m^{-1}; Figure 3b), comparable to the values from the surface samples. One suevite sample is an outlier with higher κ of 208×10^{-6} SI and NRM intensity of 5×10^{-2} A m^{-1}. Total magnetizations range from 0.06×10^{-2} to 6.30×10^{-2} A m^{-1}, averaging at ~0.014 A m^{-1}, two orders of magnitude lower than the suevite in NR73 (Table 1).

In the melt samples ($n = 28$) κ shows a broad range, but is generally higher than in the suevite (from 12×10^{-6} to 4900×10^{-6} SI, average of 943×10^{-6} SI, Figure 3e,f; Table 1). NRM intensity follows the same trend, with a wide range but generally higher values than in the suevite (from 4.4×10^{-3} to 0.5 A m^{-1}, average of 0.13 A m^{-1}; Figure 3f). Melt sample 80-II was excluded from our analysis, as it showed negative NRM and κ results. Total magnetization ranges between 0.007 and 0.55 A m^{-1}, averaging at 0.161 A m^{-1}, one order of magnitude higher than the suevites from SUBO, but one order of magnitude lower than the suevites of NR73 (see compare Figure 3b,f; Table 1).

Magnetic Grain Size and Magnetic Component Analysis

Hysteresis data are plotted in a Day diagram (Day et al., 1977; Figure 4) showing the M_{rs}/M_s and B_{cr}/B_c ratios, which are distributed along the MD-SD (single-domain) mixing lines of magnetite (Dunlop, 2002). IRM

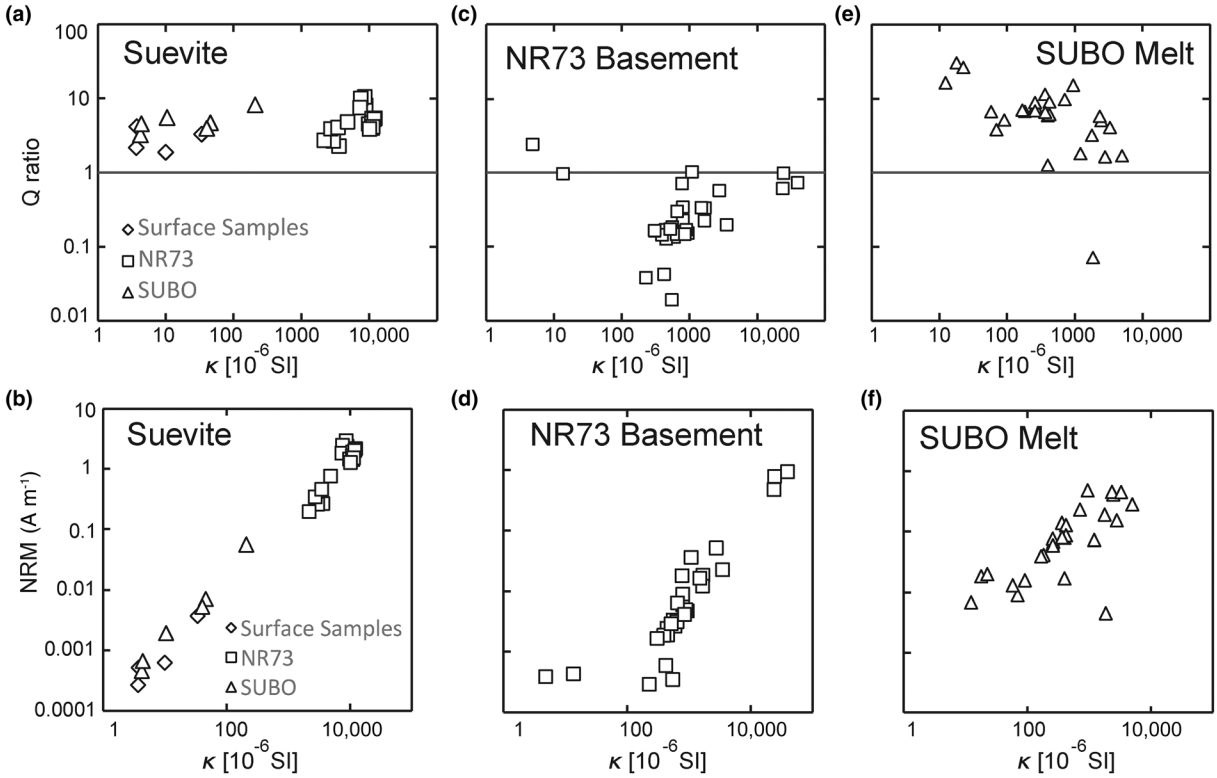

FIGURE 3. Rock magnetic properties: κ = Magnetic susceptibility (SI); Natural remanent magnetization (NRM) intensity (A m^{-1}); Koenigsberger (Q-) ratios, by sample lithology. (a) Suevite samples all demonstrate the NRM control of magnetization ($Q > 1$); (b) suevite samples show very strong NRM and κ in the NR73 suevites, and similar values in the suevites in SUBO-18 and surface samples; (c) basement of NR73 demonstrates induced magnetization is the main control of magnetization ($Q < 1$); (d) intensity of NRM and κ values are strongly reduced in the basement; (e) SUBO-18 melt samples demonstrate the NRM control of magnetization; (f) SUBO-18 met samples demonstrate generally low NRM intensities and intermediate κ.

component analysis is presented as gradient acquisition plots (GAPs), and complimentary linear acquisition plots (LAPs) in Figure 5. Table 2 shows average coercivity of remanence ($B_{1/2}$, shortened to "coercivity" for easier readability) and component contribution to the total magnetization signal [%]. File S3 has all IRM and hysteresis data used in this section, including Table S3, which contains extra parameters for each sample.

Surface Samples

The suevite surface samples show PSD behavior in the Day diagram (Figure 4), and three out of four samples possess a single component of magnetization with average coercivity between 40 and 52 mT, which is interpreted as PSD magnetite (Figure 5, Table 2). The melt-rich Polsingen sample shows a second high coercivity (1778 mT) component with a contribution of 36%, which we interpret as hematite.

NR73

The basement samples from NR73 show PSD behavior (Figure 4), with generally low M_{rs}/M_s values (<0.2), and two outlier samples that move further into the MD + PSD area (Figure 4). Suevite samples also show PSD behavior, despite a wider distribution and a trend to higher M_{rs}/M_s values (Figure 4). IRM component analysis does not show a clear distinction from suevite, with 30 out of 35 analyzed samples showing a single component, with coercivity ranging between 23 and 68 mT (average of 40 mT). Five samples show two components, three of which show a 13%–25% high-coercivity component contribution (1000–1412 mT), which we interpret as hematite. One suevite sample shows a medium-coercivity component (200 mT) with a contribution of 17%, which we interpret potentially as Ti-maghemite (Table 2).

SUBO

Suevite samples from SUBO show similar apparent PSD domain state, but generally with higher M_{rs}/M_s than the NR73 suevites (Figure 4). IRM component analysis suggests a single component of magnetization with coercivity ranging from 55 to 87 mT, averaging at 68 mT. This phase is interpreted as high-coercivity magnetite,

TABLE 1. Rock magnetic parameters.

Sample	κ (SI)	(κ*B)	NRM (A m^{-1})	Q	M_t (A m^{-1})
Surface samples					
Altenburg	9.98E-06	0.0003	0.0006	1.87	0.001
Aumühle	3.70E-06	0.0001	0.0003	2.17	0.000
Polsingen	3.38E-05	0.0011	0.0037	3.30	0.005
Wengenhausen	3.75E-06	0.0001	0.0005	4.15	0.001
SUBO					
SUBO-22	4.23E-06	0.0001	0.000	3.23	0.001
SUBO-24	4.39E-06	0.0001	0.001	4.55	0.001
SUBO-33	1.05E-05	0.0003	0.002	5.55	0.002
SUBO-38-I	2.08E-04	0.0068	0.056	8.20	0.063
SUBO-38-II	4.56E-05	0.0015	0.007	4.69	0.009
SUBO-40	4.03E-05	0.0013	0.005	3.95	0.007
SUBO-50-I	2.57E-04	0.0084	0.062	7.38	0.071
SUBO-50-II	6.98E-05	0.0023	0.009	3.83	0.011
SUBO-50-III	3.98E-04	0.0131	0.077	5.91	0.091
SUBO-50-IV	5.80E-05	0.0019	0.013	6.70	0.015
SUBO-50-V	1.80E-05	0.0006	0.018	30.42	0.019
SUBO-51-I	1.83E-04	0.0060	0.041	6.76	0.047
SUBO-51-II	2.63E-04	0.0086	0.068	7.83	0.076
SUBO-52-I	1.67E-04	0.0055	0.039	7.03	0.044
SUBO-52-II	2.58E-04	0.0085	0.076	8.91	0.084
SUBO-71	7.11E-04	0.0234	0.228	9.76	0.252
SUBO-73	2.26E-05	0.0007	0.020	26.32	0.020
SUBO-80-I	9.47E-04	0.0312	0.476	15.26	0.507
SUBO-84	3.63E-04	0.0120	0.138	11.53	0.150
SUBO-85	1.23E-05	0.0004	0.007	16.43	0.007
SUBO-86	1.85E-03	0.0610	0.004	0.07	0.065
SUBO-87	9.11E-05	0.0030	0.015	5.17	0.018
SUBO-89-I	4.00E-04	0.0132	0.017	1.27	0.030
SUBO-89-II	2.46E-03	0.0810	0.409	5.05	0.490
SUBO-90	2.34E-03	0.0770	0.448	5.82	0.525
SUBO-91	4.22E-04	0.0139	0.126	9.10	0.140
SUBO-92-I	4.98E-03	0.1641	0.278	1.69	0.442
SUBO-92-II	2.59E-04	0.0085	0.058	6.86	0.067
SUBO-93	4.21E-04	0.0139	0.085	6.14	0.099
SUBO-95-II	2.79E-03	0.0919	0.151	1.65	0.243
SUBO-95-II	3.29E-03	0.1084	0.444	4.09	0.552
SUBO-97	3.66E-04	0.0120	0.079	6.59	0.091
SUBO-98	1.21E-03	0.0397	0.072	1.81	0.111
SUBO-100	1.79E-03	0.0589	0.189	3.21	0.248
NR73					
NR73-332 S	3.6E-03	0.1172	0.268	2.28	0.385
	2.9E-03	0.0968	0.259	2.67	0.355
NR73-376 S	1.1E-02	0.3621	1.437	3.97	1.799
	8.9E-03	0.2913	2.367	8.13	2.658
	8.5E-03	0.2811	2.968	10.56	3.249
	7.4E-03	0.2446	2.455	10.04	2.700
	7.3E-03	0.2396	1.816	7.58	2.056
NR73-475 S	1.1E-02	0.3621	1.899	5.25	2.261
	1.1E-02	0.3588	1.920	5.35	2.279
	1.2E-02	0.3983	2.167	5.44	2.565

TABLE 1. *Continued.* Rock magnetic parameters.

Sample	κ (SI)	(κ*B)	NRM (A m^{-1})	Q	M_t (A m^{-1})
NR73-498 SG	9.7E-03	0.3203	1.461	4.56	1.781
	1.1E-02	0.3555	1.662	4.68	2.017
	1.2E-02	0.3884	2.039	5.25	2.427
	1.1E-02	0.3686	1.531	4.15	1.900
	1.0E-02	0.3291	1.279	3.89	1.608
NR73-528 Gn	9.3E-04	0.0308	0.005	0.15	0.035
NR73-529 Gn	5.9E-04	0.0195	0.003	0.14	0.022
NR73-530 Gn	3.9E-02	1.2869	0.943	0.73	2.230
NR73-530 Gn-II	7.9E-04	0.0261	0.006	0.23	0.032
NR73-534 Gn	1.7E-03	0.0553	0.018	0.33	0.074
NR73-535 Gn	1.1E-03	0.0356	0.036	1.02	0.072
NR73-536 Gn	2.8E-03	0.0905	0.052	0.57	0.143
NR73-539 Gn	2.3E-04	0.0075	0.000	0.04	0.008
NR73-540 SG	4.2E-04	0.0139	0.001	0.04	0.014
NR73-546 SG	3.5E-03	0.1155	0.023	0.20	0.138
NR73-552 SG	8.0E-04	0.0262	0.009	0.34	0.035
NR73-557 Gn	5.5E-04	0.0182	0.003	0.18	0.022
NR73-573 Gn	8.9E-04	0.0294	0.005	0.17	0.034
NR73-574 Gn	4.4E-04	0.0145	0.002	0.17	0.017
NR73-612 Gn	1.7E-03	0.0546	0.012	0.22	0.067
NR73-617 A	4.5E-04	0.0148	0.002	0.13	0.017
	3.9E-04	0.0129	0.002	0.15	0.015
NR73-621 Gn	6.4E-04	0.0211	0.003	0.15	0.024
NR73-623 Gn	6.5E-04	0.0215	0.006	0.30	0.028
NR73-624 Gn	1.4E-05	0.0004	0.000	0.97	0.001
NR73-629 Gn	4.8E-06	0.0002	0.000	2.42	0.001
NR73-630 Gn	2.4E-02	0.7801	0.477	0.61	1.257
	2.4E-02	0.7998	0.787	0.98	1.586
NR73-664 Gn	7.7E-04	0.0254	0.018	0.71	0.044
NR73-672 Gn	5.2E-04	0.0170	0.003	0.17	0.020
NR73-680 SG	2.2E-03	0.0711	0.195	2.75	0.266
	2.7E-03	0.0889	0.346	3.90	0.435
	3.4E-03	0.1132	0.461	4.08	0.575
	4.8E-03	0.1573	0.764	4.86	0.922
NR73-820 MB	5.5E-04	0.0180	0.000	0.02	0.018
NR73-826 MB	3.0E-04	0.0100	0.002	0.16	0.012
NR73-827 MB	8.5E-04	0.0280	0.004	0.15	0.032
NR73-829 MB	1.5E-03	0.0492	0.017	0.34	0.066

Abbreviations: κ, magnetic susceptibility; κ*B, induced magnetization; NRM, natural remanent magnetization; Q, Koenigsberger ratio; M_t, total magnetization, given by NRM + κ*B.

suggesting magnetic domain states of fine PSD or SD. All melt samples show a mean component coercivity ranging from 40 to 112 mT (average at 68 mT, similar to the suevites), which we also interpret as relatively fine PSD or SD magnetite. Twenty-two out of 34 samples show a second component, which we separate into two categories: "medium-coercivity" (200–500 mT) and "high-coercivity" (500–1258 mT). Ten samples show the "medium-coercivity" component, which we interpret as being potentially Ti-maghemite with contributions ranging from 5% to 12%. The "high-coercivity" component is present in 12 samples, which we interpret as hematite, with contributions between 5% and 34%. Melt samples generally show high coercivity PSD state behavior in the Day diagram, with some plotting close to the PSD + SD area, suggesting fine magnetic grain sizes (Figure 4). The results from both suevite and melt in SUBO do not fit within the SD-MD mixing lines from Dunlop (2002; Figure 4), likely due to the presence of a significant amount of non-magnetite components, which limits the interpretations that can be made from the Day diagram (see Roberts et al., 2018). For this reason, we evaluate the domain state primarily from high-coercivity results of the IRM modeling.

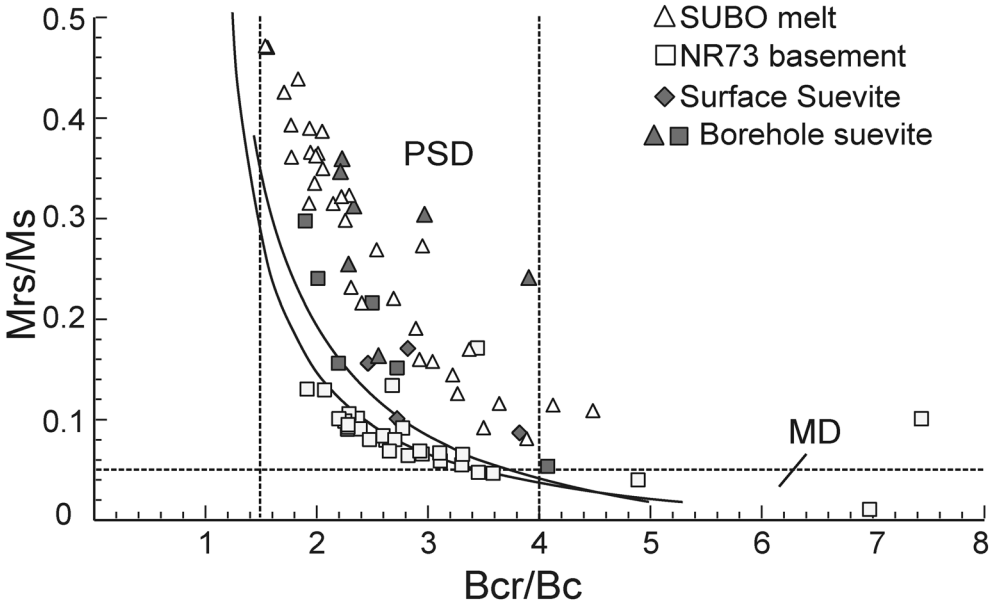

FIGURE 4. Day diagram (Day et al., 1977) with SD-MD mixing lines (Dunlop, 2002) for hysteresis data of our samples. MD, multidomain; PSD, pseudo-single domain; SD, single domain. Note a preferential close clustering of domain states in the basement of NR73 along the SD-MD mixing lines, and a tendency of SUBO melts toward PSD + SD mixed compositions.

Texture and Composition of Magnetic Phases

Surface Samples

In the Altenbürg suevite the main magnetic phase is magnetite, with small and round void-filling skeletal textures, and grain sizes ranging from ~5 to 10 µm, often grown in multigrain clusters up to 50 µm in diameter (Figure 6a). In this suevite, some very rare fractured magnetite grains (~40 µm) were also observed. EPMA indicates that the non-fractured granular grains show compositions near magnetite ($Fe_{2.86}Al_{0.02}Ti_{0.01}Mg_{0.01}O_4$, $n = 32$) with a small amount of vacancies (Vacancies = 0.1, see Table 3), indicating some cation deficiency. Vacancies are formed from the oxidation of ferrous Fe due to low-temperature hydrothermal alteration or weathering according to: $2\ Fe^{2+} = Fe^{3+} + \text{vacancy}$ (Dunlop & Ozdemir, 2000). These results suggest some degree of maghemitization of magnetite.

The very melt-rich suevite samples from Polsingen present both magnetite and hematite as the main magnetic phases according to our rock magnetic data. Macroscopically, the samples show a red color, while microscopically hematite shows skeletal (~5 µm) growth around and along fractures in quartz crystals. Other oxides contain very high Ti concentrations, and are grown as skeletal grains and "clusters" similar to magnetite in the Altenbürg suevite (Figure 6b). EPMA of suitable grains ($n = 6$) suggests this is a member of the pseudobrookite series ($Fe_{1.89}Ti_{0.67}Mg_{0.16}Al_{0.05}Mn_{0.01}O_5$; File S4, and Table S4).

Aumühle suevite does not show any microscopically visible magnetic phase. The Fe-rich phase in this sample consists of cation-substituted and cation-deficient ilmenite ($Ti_{0.89}Fe_{0.67}Mg_{0.03}Mn_{0.01}O_3$, $n = 36$; Figure 6c; File S4, and Table S4).

NR73

The main magnetic phase in all lithologies of NR73 is magnetite. In suevite, there is a mix of inherited, shock-fractured magnetite from the basement, and newly formed magnetite. The new magnetite is generally idiomorphic and non-fractured, with grain sizes ranging from ~5 µm up to ~100 µm (Figure 6d). Like in surface suevite, some fractured basement magnetite grains are also found. EPMA ($n = 14$) shows low cation substitution in this magnetite ($Fe_{2.99}Ti_{0.01}O_4$) and no vacancies (Table 3). However, one spot measurement indicated that locally some of these non-fractured magnetite grains may show a higher cation substitution ($Fe_{2.68}Ti_{0.12}Mn_{0.01}Al_{0.01}O_4$), but these grains are very rare (only once observed, see File S4 and Table S4).

In the gneiss basement, the magnetite grains are fractured and larger than in the suevite (up to ~200 µm; see Figure 6e,f). These grains often show ilmenite either filling the fractures in magnetite (see Figure 6e), or intergrown with magnetite (Figure 6f), suggesting that some of the ilmenite is secondary and post-impact. EPMA shows that magnetite compositions range from $Fe_{3.02}Cr_{0.01}Al_{0.01}Ti_{0.01}O_4$ to $Fe_{2.93}Ti_{0.01}Al_{0.01}O_4$ (in two samples with $n = 15$ and $n = 10$, see Table 3), with a low

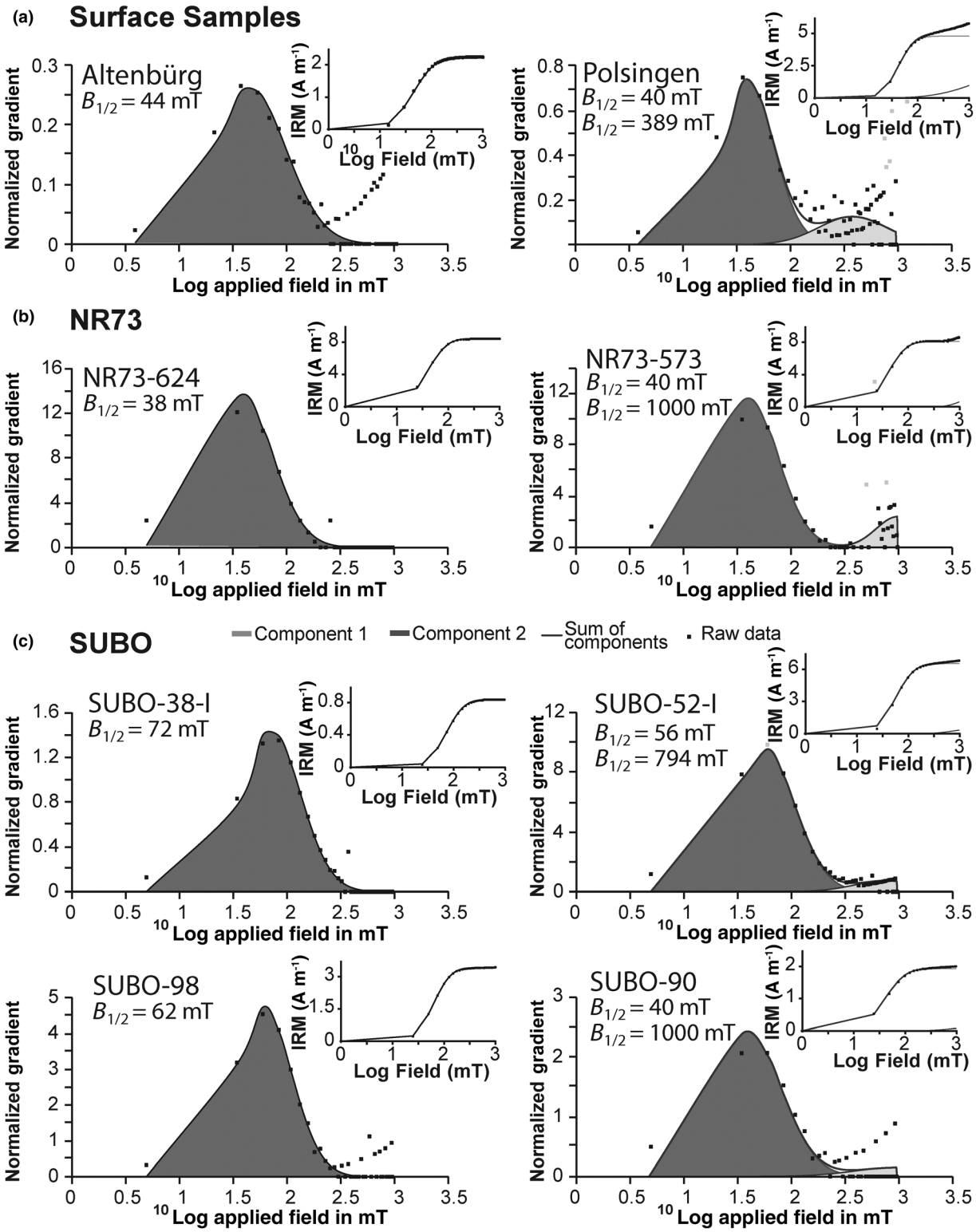

FIGURE 5. IRM component analysis GAP and LAP for representative samples; (a) Surface samples with one (left) and two (right) components; (b) NR73 shocked magnetite with one (left) and two (right) components; (c) SUBO suevite samples with one and two components (top left and right, respectively), and SUBO melt samples with one and two components (bottom left and right, respectively).

TABLE 2. IRM modeling component contribution and average grain population coercivity ($B_{1/2}$) for all our samples, see text for details.

	Component 1		Component 2	
	Cont. (%)	B(1/2) (mT)	Cont. (%)	B(1/2) (mT)
Surface samples				
Altenbürg	100	43.7	—	—
Aumühle	100	52.5	—	—
Polsingen	64	41.7	36	1778.3
Wengenhausen	100	39.8	—	—
NR73				
NR73-332 S	100	67.6	—	—
NR73-376 S	83	44.7	17	199.5
NR73-475 S	100	57.5	—	—
NR73-498 SG	100	57.5	—	—
NR73-528 Gn	100	41.7	—	—
NR73-529 Gn	100	36.3	—	—
NR73-530 Gn	100	38.0	—	—
NR73-530 Gn-II	100	33.1	—	—
NR73-534 Gn	100	43.7	—	—
NR73-535 Gn	100	28.2	—	—
NR73-536 Gn	100	30.2	—	—
NR73-539 Gn	100	42.7	—	—
NR73-540 Gn	100	40.7	—	—
NR73-546 S	100	38.0	—	—
NR73-552 SG	87	39.8	13	1000.0
NR73-557 S	100	35.5	—	—
NR73-557 G	100	35.5	—	—
NR73-573 Gn	100	25.1	—	—
NR73-574 Gn	86	33.9	14	1412.5
NR73-612 Gn	100	28.8	—	—
NR73-617 A	75	63.1	25	1000.0
NR73-621 Gn	100	33.1	—	—
NR73-623 Gn	100	38.0	—	—
NR73-624 Gn	100	39.8	—	—
NR73-629 Gn	50	36.3	50	398.1
NR73-630 Gn	100	40.7	—	—
NR73-664 Gn	100	33.9	—	—
NR73-672 Gn	100	31.6	—	—
NR73-680 SG	100	29.5	—	—
NR73-820 MB	100	60.3	—	—
NR73-826 MB	100	22.9	—	—
NR73-827 MB	100	28.2	—	—
NR73-829 MB	100	30.9	—	—
SUBO				
SUBO-22	100	83.2	—	—
SUBO-24	100	87.1	—	—
SUBO-33	91	57.5	9	223.9
SUBO-38-I	100	72.4	—	—
SUBO-38-II	100	55.0	—	—
SUBO-40 g	100	58.9	—	—
SUBO-40 m	100	58.9	—	—
SUBO-50-I	100	69.2	—	—
SUBO-50-II	100	66.1	—	—
SUBO-50-III	100	60.3	—	—
SUBO-50-IV	88	44.7	12	398.1
SUBO-50-V Red	88	63.1	12	446.7
SUBO-50-V Wht	100	70.8	—	—
SUBO-51-I	92	56.2	8	251.2
SUBO-51-II	96	60.3	4	794.3
SUBO-52-I	93	56.2	7	794.3
SUBO-52-II g	80	60.3	20	1258.9
SUBO-52-II m	100	66.1	—	—
SUBO-71	95	97.7	5	794.3
SUBO-73	90	89.1	10	1000.0
SUBO-80-I	93	74.1	7	501.2
SUBO-80-II	94	69.2	6	501.2
SUBO-84 Gn	95	100.0	5	501.2
SUBO-84 M	84	79.4	16	489.8
SUBO-85	100	93.3	—	—
SUBO-86	100	75.9	—	—
SUBO-87	88	72.4	12	631.0
SUBO-89-I Gn	100	95.5	—	—
SUBO-89-I M	76	47.9	24	707.9
SUBO-89-II	91	74.1	9	1000.0
SUBO-90	93	39.8	7	1000.0
SUBO-91	100	66.1	—	—
SUBO-92-I	95	44.7	5	251.2
SUBO-92-II	100	70.8	—	—
SUBO-93	95	67.6	5	316.2
SUBO-95-II	90	47.9	10	794.3
SUBO-95-II	66	46.8	34	933.3
SUBO-97	100	63.1	—	—
SUBO-98	100	61.7	—	—
SUBO-100	94	61.1	6	1000.0

vacancy concentration (0–0.05). Secondary ilmenite shows a range of compositions from $Ti_{0.76}Fe_{0.73}Mn_{0.24}O_3$ to $Fe_{0.86}Ti_{0.85}Mn_{0.12}O_3$ (File S4 and Table S4).

Magnetite from the metabasite basement shows a very chromium-rich composition ($n = 10$, $Fe_{2.86}Cr_{0.11}Ti_{0.01}O_4$) and in average a vacancy concentration of 0.13. These magnetite grains occur as dusty grains in silicates (~5–10 μm) and as lightly fractured larger xenomorphic grains (~100 μm) between silicate crystals, fractured during impact (Figure 6g), which we interpret as preserved primary magmatic or metamorphic textures of pre-impact origin. Cation-substituted and cation-deficient ilmenite

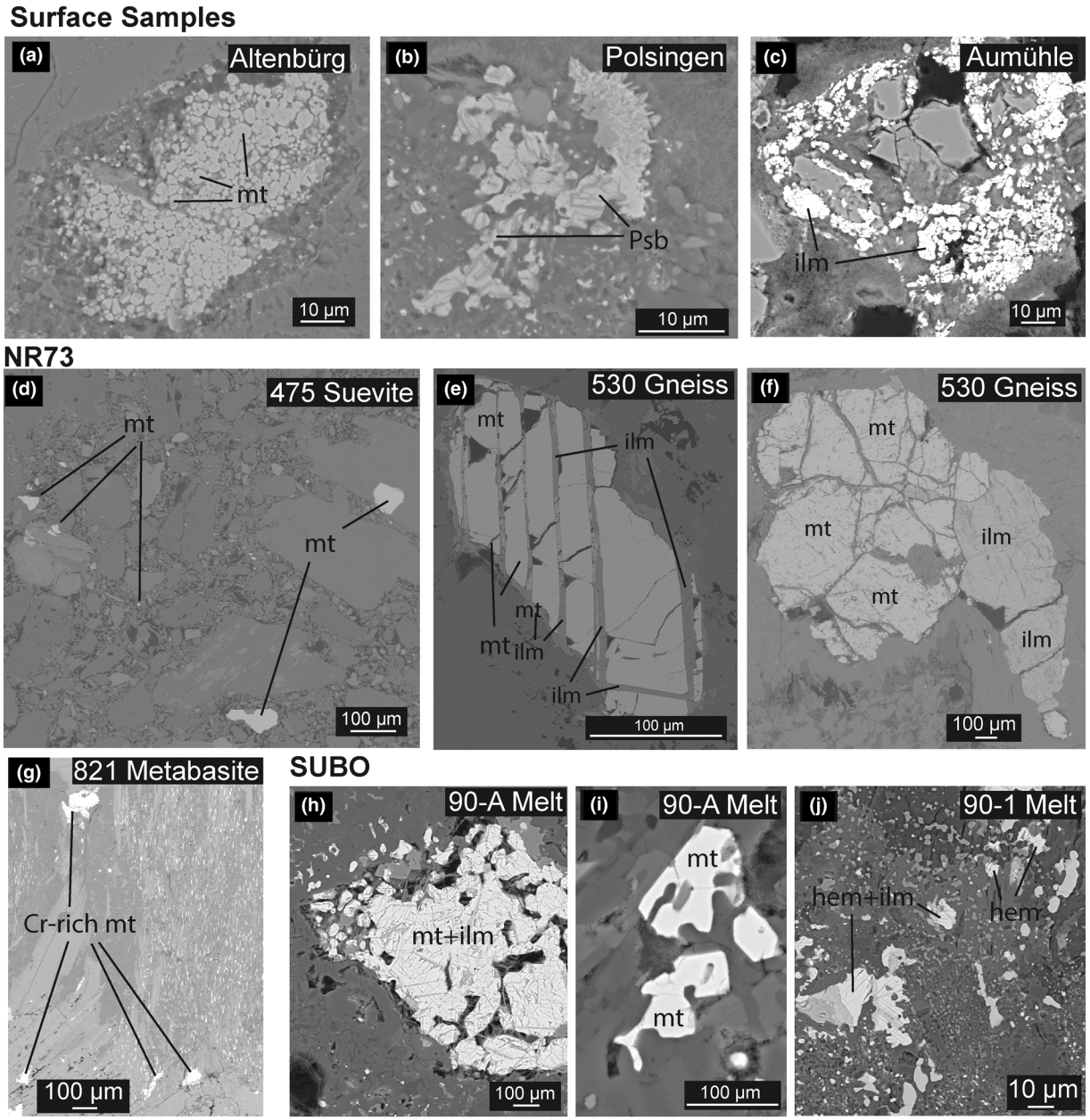

FIGURE 6. Backscattered electron images obtained from electron probe microanalysis (EPMA) of representative grains. hem, hematite; ilm, ilmenite; mt, magnetite; and psb, pseudobrookite. (a) Small and round, void-filling grains, melt-derived, from Altenbürg; (b) void-filling textured pseudobrookite series grain in the Polsingen melt sample; (c) secondary ilmenite deposited along cracks of fractured grains in suevite from Aumühle; (d) small, newly formed magnetite grains in the suevite of NR73; (e) fractured magnetite grain in the basement of NR73—note the ilmenite deposited in shock fractures of magnetite; (f) shock-fractured magnetite and shocked-fractured primary ilmenite intergrowth in the basement of NR73; (g) Cr-rich skeletal grains in the metabasite sample in NR73; (h–j) Examples of suitable, larger-than-usual grains that allowed for EPMA, from the SUBO melt sample 90.

($Ti_{0.91}Fe_{0.73}Mn_{0.16}Mg_{0.01}O_3$, $n = 15$) is also present in the metabasite with textures similar to the magnetite, suggesting a congenic formation of both Fe-oxide phases.

SUBO

In the suevite and melt-rich suevite sections (21.19–86.24), mostly pyrite and Fe-carbonates occur (see raw and EDX data in File S3—EPMA). When Fe-oxides are

TABLE 3. Averaged electron probe microanalysis data, in wt% and cation contribution per formula unit of surface, NR73, and SUBO-18 samples, refer to text or details. Standard deviations (1 s) are provided within parenthesis.

	Altenbürg	NR73-475 S	475 Ti-rich	NR73-530 Gn	NR73-530 Gn-II	NR73-821 MB	SUBO-90
n	32	14	1	15	10	10	7
O	28.09 (1.56)	27.36 (0.56)	28.82	27.21 (0.58)	28.4 (0.49)	27.58 (0.58)	27.91 (1.17)
Cr	0.05 (0.03)	0.07 (0.04)	0.02	0.24 (0.02)	0.03 (0.01)	2.56 (0.51)	0.06 (0.07)
Fe	69.83 (2.00)	71.4 (0.43)	67.46	71.65 (0.35)	67.2 (0.20)	68.87 (0.80)	66.69 (2.29)
Mn	0.07 (0.04)	0.05 (0.04)	0.35	0.02 (0.01)	0.89 (0.02)	0.10 (0.03)	0.11 (0.09)
Al	0.24 (0.19)	0.04 (0.03)	0.11	0.09 (0.04)	0.11 (0.05)	0.023 (0.01)	0.56 (0.48)
Mg	0.13 (0.08)	0.01 (0.01)	n.d.	n.d.	0.01 (0.00)	0.02 (0.00)	0.13 (0.10)
Ti	0.19 (0.29)	0.12 (0.11)	2.54	0.11 (0.04)	2.62 (0.10)	0.13 (0.04)	1.60 (1.00)
Total	98.61 (0.45)	99.06 (0.67)	99.31	99.32 (0.65)	99.27 (0.67)	99.29 (0.81)	97.07 (0.72)
Cr	—	—	—	0.01 (0.00)	—	0.11 (0.02)	—
Fe^{2+}	1.41 (0.00)	1.41 (0.00)	1.41	1.41 (0.00)	1.41 (0.00)	1.41 (0.00)	1.41 (0.00)
Fe^{3+}	1.45 (0.21)	1.58 (0.10)	1.27	1.61 (0.07)	1.52 (0.05)	1.45 (0.06)	1.34 (0.21)
Mn	—	—	0.01	—	—	—	—
Al	0.02 (0.01)	—	0.01	0.01 (0.00)	0.01 (0.00)	—	0.05 (0.04)
Mg	0.01 (0.01)	—	—	—	—	—	0.01 (0.01)
Ti	0.01 (0.01)	0.01 (0.03)	0.12	0.01 (0.00)	0.01 (0.00)	0.01 (0.00)	0.08 (0.05)
O	4.00	4.00	4.00	4.00	4.00	4.00	4.00
# Cations	2.90	3.00	2.82	3.04	2.95	2.87	2.89
Vacancies	0.10	—	0.18	—	0.05	0.13	0.11
T_c Calc (4O)	574	576	513	576	573	576	537
T_c Measured	572	574	574	578	578	556	541

Note: Formulas were calculated assuming four oxygen anions. Standard deviations (1 s) are given in parenthesis.

present, only very small hematite grains are identified. Only in the continuous impact melt rock (86.24–99.98), sample 90 shows magnetite grains large enough to be measured by EPMA. Most of the grains are very small (~5–10 μm) with some exceptions where measurement is possible (Figure 6h,i). These grains are not fractured, show globular shapes that appear to fill pore spaces (Figure 6h, i), and are often intergrown with other oxides, generally hematite and ilmenite (Figure 6h,j, see File S4, Table 2). Where magnetite was observed, the compositions are slightly cation-substituted ($Fe_{2.75}Ti_{0.08}Al_{0.05}Mg_{0.01}O_4$) and cation-deficient (vacancies = 0.11).

In addition to chemical composition, Table 3 shows the calculations of expected Curie temperatures for each composition, using the empirical formula described in Engelmann (2008) for comparison with the measured Curie temperature.

Magnetic Transition temperatures

Classification of κ–T *Curves*

We subdivided four different types according to their main features in the heating κ–T curves. Frequently the κ–T curves are irreversible, with the heating curves reflecting the original magnetic phases. Mineral reactions during heating may mask this phase in the cooling curve, which in turn provides insight into the alteration of the sample.

Type 1 shows paramagnetic behavior in the LT measurement and heating curve. We classify a curve as *type 1a* if both heating and cooling curves are reversible and paramagnetic (see "AUM1—Type 1a", in Figure 7a). *Type 1b* curves show paramagnetic behavior in the heating curve, but irreversible cooling curves with a strong increase in κ, a large bump between around 200 and 400°C, and generally a A40 >100% (e.g., "WEN1—Type 1b", Figure 7a), indicating the formation of a ferrimagnetic phase during the measurement.

Type 2 and *type 3* (*3a* and *3b*) refer to (Ti-)magnetite, usually presenting Verwey transitions between −147 and −175°C; and Curie temperatures between 545 and 604°C, depending on cation substitution and oxidation. *Type 2* curves are mostly reversible (Figure 7b), while *type 3* is irreversible (Figure 7c). *Type 3a* refers to irreversible (Ti-) magnetite that shows stable κ from RT to the Curie temperature (Figure 7d), while *type 3b* refers to samples with constant κ increase from RT to Hopkinson peak (Figure 7e), generally attributed to very small SD magnetite grains. *Type 3a* can present two types of irreversibility in NR73, those with a κ decrease after heating (negative A40; Figure 7c) or increase (positive A40, Figure 7d,e).

Type 4 shows at least two ferrimagnetic phases, attributed to different (Ti-)magnetite compositions with varying rates of cation substitution, causing the presence of two different T_c (see two examples in Figure 7d).

We further subdivided the curves into subtypes "O" and "R", depending on their alteration during the κ–T experiment expressed in the cooling curves.

Subtype "O" is characterized by a "hump" in κ between 200 and 350°C in the heating curve. Samples with this behavior may show typical (Ti-)magnetite characteristics (e.g., a "3a-O" type), with this "hump" which we associate with transformation of maghemite to magnetite during the experiment (Figure 7d).

Subtype "R" is irreversible and characterized by a very sharp Curie temperature at ~320°C in the cooling curve, which we associate with the formation of pyrrhotite from pyrite during the heating experiment in an argon atmosphere (Figure 7e).

These alterations mainly pertain to the maghemitization of magnetite, or the presence of secondary pyrite in the samples, both of which are diagnostic of hydrothermal alteration. Thus, this subdivision allows us to constrain the hydrothermal conditions ("O" = Oxidizing; "R" = Reducing).

File S5 contains all κ–T curves for the surface samples, NR73 and SUBO.

Surface Samples

The Altenbürg suevite ($n = 2$) shows no clear Verwey transition in the first low temperature measurement, but it appears as a broad transition around −175°C (Table 4) in a second low temperature measurement after heating to 700°C. Both measured samples are classified as type 3a-O. The Curie temperature at ~570°C is sharp and reversible, in accordance with the T_c calculated from chemical composition (see Table 3). The cooling curve shows an increase in κ below 400°C, causing an A40 = ~47% (Table 4).

Both the Polsingen melt and melt-rich suevite are classified as type 3b-O. A Verwey transition at −165°C can be observed. Curie temperatures of both samples are around 576°C (Table 4), and κ–T curves are reversible in both melt and melt-rich suevite samples, suggesting no difference in the magnetic carriers of melt and suevite.

Both samples in Aumühle and Wengenhausen belong to type 1, with fully paramagnetic behavior. Aumühle is a type 1a sample, while Wengenhausen samples show a large positive A40 (Figure 7a, Table 4). A repeated κ–T curve was done for a second Wengenhausen sample (WEN2-1-1 and 2-2; Table 4 and Table S5), where the shape of WEN2-1's cooling curve was maintained in WEN2-2, indicating that the newly formed ferrimagnetic phase is stable at RT conditions. We suggest that in Wengenhausen, the signal is due to Fe-carbonate alteration into a ferrite of presumably mixed cation (e.g., Fe, Mn, Mg, and Ca) composition during the first κ–T experiment.

NR73

In the NR73 drill core ($n = 41$), the majority of the κ–T curves belong to either type 2 ($n = 7$) or type 3 ($n = 24$), indicating that (Ti-)magnetite is the main carrier of magnetization both in the suevite and in the basement. Type 1 samples are also common ($n = 7$), and four consist of type 1b. In the lowest sections of the core, type 4 curves can be identified ($n = 3$), with at least two types of cation-substituted magnetite contributing to the magnetization of the sample (see example in Figure 7d; in Table 4, notice the two Curie temperatures in heating and cooling curves from the type 4 metabasite samples).

In the suevites, four out of seven samples show hydrothermal alteration, with three "3b-O" subtype in the lower sections of the unit, and one 3b-R curve at the contact with the basement (Table 4). The observation of type 3b in these samples suggests small SD grain sizes, in agreement with our microscopical observations (Figure 6d). All type 3 curves in the suevites show a positive A40, suggesting the formation of new ferromagnetic material, causing a 16%–55% increase in κ. Verwey transitions are ~−167°C with Curie temperatures in the heating curve around ~578°C, in agreement with the calculated from the chemical composition (Table 3).

In the basement, most samples are unaltered, with one 3a-R sample limited to a suevite dyke at 546 m depth (Table 4). Most type 3 show a decrease of κ ranging from 9% to 29%. Only one basement type 3 sample shows a 20% increase in κ. The Verwey transitions are ~−158°C, which is lower than the T_v for pure magnetite (~−153°C, Verwey, 1939), only sample 821 MB shows an even lower T_v at −180°C. The Curie temperatures average 580°C, with variations related to varying degrees of cation substitution (see calculated T_c in Table 3). Type 4 samples are limited to the lower sections of the core in the metabasite samples, where we attribute the pure magnetite T_c ~ 580°C to the dusty grains, and the second Curie temperature ranging from 440 to 529°C to the Cr-rich phases are observed (cf. calculated T_c in Tables 3 and 4; Figure 6g).

SUBO

In SUBO ($n = 35$), the most common type is also type 3 ($n = 22$), mainly type 3b, suggesting that SD (Ti-) magnetite is the main magnetic carrier, in line with previous observations (Tables 2 and 3, Figures 4–6). A wider range of cation substitution is inferred by the wider range of Curie temperatures in the heating curves, ranging from 545 to 619°C in the main magnetic phase (Table 4). The presence of type 4 samples ($n = 7$) in the

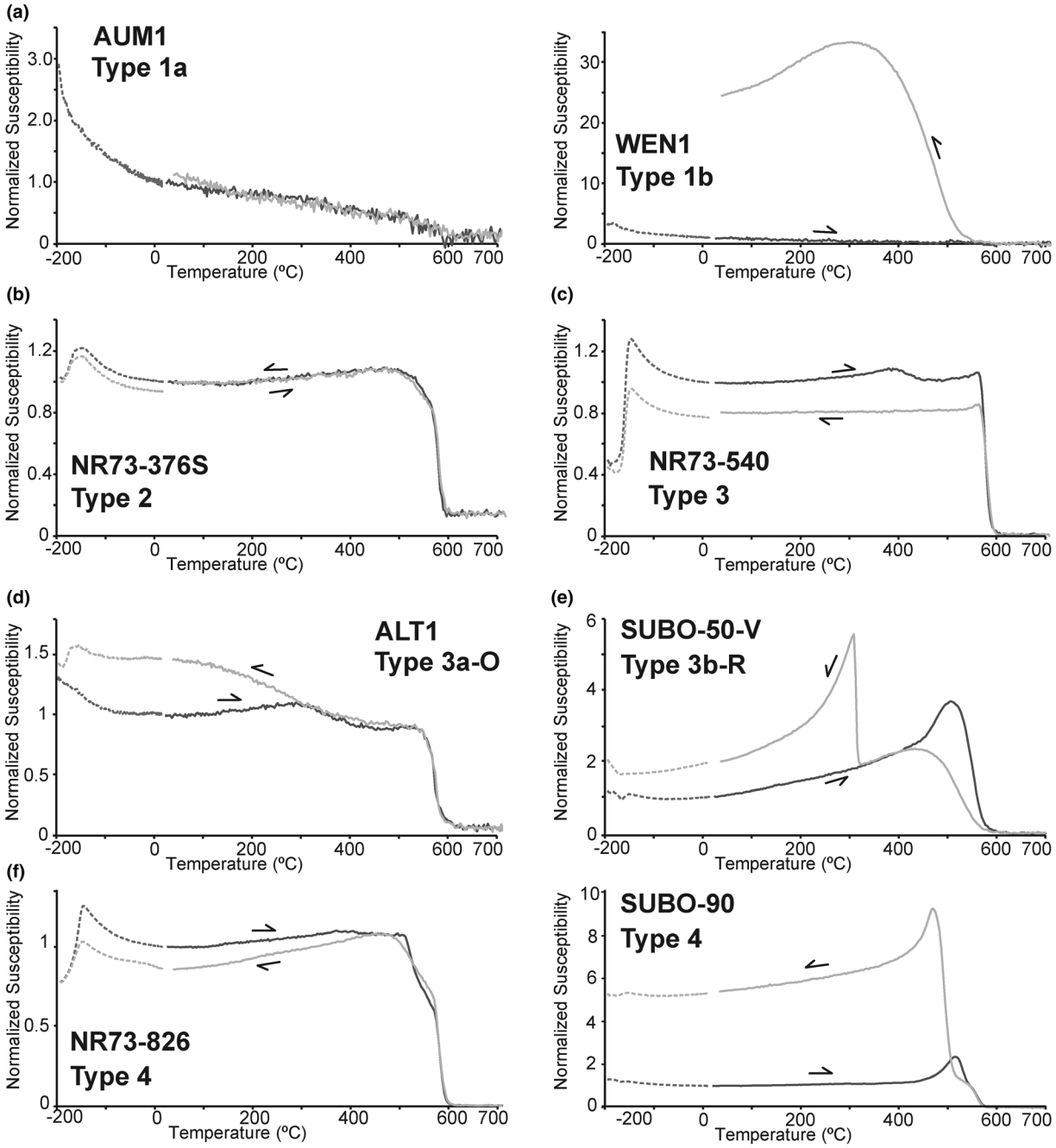

FIGURE 7. Representative κ–T curves from different types found in our samples. (a) Type 1 samples, type 1a (left) shows fully paramagnetic sample, type 1b (right) shows the formation of a new ferrimagnetic phase after an original paramagnetic curve; (b) type 2 shows a reversible κ–T curve denoting (Ti-)magnetite; (c) type 3 shows an irreversible κ–T curve denoting (Ti-)magnetite, 3b denotes a SD (Ti-)magnetite curve; (d) subtype "O" curves are characterized by a "hump" of κ between 200 and 350°C in the heating curve; (e) subtype "R" curves are characterized by a very sharp Curie temperature at ~320°C, caused by the syn-experimental formation of pyrrhotite from pyrite; (f) type 4 curves show a multi-component κ–T curve, characterized by two Curie temperatures, at 580°C, and a second, around 530°C, regardless of the shape of the curve.

melt and suevites demonstrates the range of cation substitution, where a more substituted (Ti-)magnetite creates multiple Curie temperatures, sometimes as low as 484°C (averaging at 530°C, see "T_cH2" in Table 4). After heating, the Curie temperatures are generally irreversible and tend to decrease, which may be attributed to cation order/disorder effects (e.g., Bowles et al., 2013; Jackson & Bowles, 2014). Verwey transition temperatures are

TABLE 4. Parameters obtained from κ–T measurements used in this study.

Depth [m]	Lith.	Sample	Tv1	Tv2	TcH 1	TcH 2	TcC 1	TcC 2	TcC 3	TvPR1	TvPR2	HPR1	HPR2	A40 [%]	Type	Classification
Surface samples																
Surface	Suevite	ALT 1	—	−176	572	579	—	—	—	—	1.08	—	—	46.9	3b—O	Syn + Ox
Surface	Suevite	ALT 2	—	−175	550	542	—	—	—	—	1.07	—	—	47.7	3b-O	Syn + Ox
Surface	Suevite	AUM 1	—	—	—	—	—	—	—	—	—	—	—	17.9	1a	Pm
Surface	Melt	POL-Melt	—	—	575	578	—	—	—	—	—	1.34	1.03	54.8	3b-O	Syn + Ox
Surface	Red Sue.	POL	−166	—	578	575	—	—	—	1.01	—	1.82	1.52	10.1	3b-O	Syn + Ox
Surface	Suevite	WEN 1	—	—	—	478	—	—	—	—	—	—	—	2319.4	1b	Pm + Ox
Surface	Suevite	WEN 2-1	—	—	566	321	—	—	—	—	—	1.10	1.41	3880.4	1b	Pm + Ox
Surface	Suevite	WEN 2-2	—	—	486	493	—	—	—	—	—	—	—	−28.9	—	—
SUBO																
22	Suevite	SUBO-22	—	−177	570	—	567	—	—	—	1.07	—	1.71	2811.8	1b	Pm + Ox
24	Suevite	SUBO-24	—	−153	533	—	569	—	—	—	1.11	6.12	1.42	1206.2	1b	Pm + Ox
33	Suevite	SUBO-33	—	−174	569	—	575	310	—	—	1.57	—	1.34	1524.8	1b-R	Pm+ R.O.
38	Suevite	SUBO-38-I	−167	—	546	—	532	323	—	1.01	—	2.76	—	7.3	3b-R	Syn-Red
38	Suevite	SUBO-38-II	−163	—	571	—	578	532	387	0.93	—	1.77	—	112.0	3b-R	Syn-Red
40	Suevite	SUBO-40	−169	—	579	547	529	—	—	1.82	—	3.61	3.08	11.2	4	Syn
50	Suevite	SUBO-50-I	−167	—	573	533	575	521	312	0.85	—	2.54	—	64.0	4-R	Syn-Red
50	Suevite	SUBO-50-II	−167	—	573	536	575	508	312	0.91	—	2.66	—	62.5	4-R	Syn-Red
50	Suevite	SUBO-50-III	−168	—	545	—	536	325	—	1.00	—	2.77	—	4.8	3b-R	Syn-Red
50	Suevite	SUBO-50-IV	−169	—	545	—	550	—	—	1.01	—	2.51	2.11	−1.5	3b	Syn
50	Suevite	SUBO-50-V	−164	—	564	—	533	321	—	1.08	—	3.68	—	93.2	3b-R	Syn-Red
51	B+Melt	SUBO-51-I	−162	—	562	—	576	532	335	0.89	—	2.49	—	157.2	3b-R	Syn-Red
51	B + Melt	SUBO-51-II	−157	—	578	—	622	528	—	0.85		2.56	—	64.4	3b-O	Syn+Ox
52	B + Melt	SUBO-52-I	−157	—	560	—	575	540	423	1.45	—	2.18	—	69.1	3b-O	Syn+Ox
52	B + Melt	SUBO-52-II	−164	−146	572	537	580	529	307	0.94	0.90	2.75	—	29.7	4-R	Syn-Red
71	B + Melt	SUBO-71	—	—	605	—	579	413	—	—	—	2.05	—	38.9	1a	Pm
73	Clast	SUBO-73	−191	−180	586	—	551	326	—	1.24	1.02	5.56	—	286.2	3b-R	Syn-Red
80	Melt	SUBO-80-I	—	—	566	—	321	—	—	—	—	5.37	—	108.4	3b-R	Syn-Red
80	Clast	SUBO-80-II	—	—	561	—	321	—	—	—	—	—	—	428.2	1a+R	Pm + Red
84	Melt	SUBO-84 M	—	—	523	—	414	—	—	—	—	—	—	1726.7	1b	Pm + Ox
84	Clast	SUBO-84 Gn	−173	−191	588	484	540	—	387	1.28	—	—	—	225.5	4	Syn
85	Melt	SUBO-85	−155	−152	576	—	577	535	313	1.28	0.92	5.05	—	617.8	3b-R	Syn-Red
86	Melt	SUBO-86	—	−151	588	—	585	466	321	—	0.98	5.84	—	880.2	3b-R	Syn-Red
87	Melt	SUBO-87	—	—	587	—	639	300	—	—	—	—	—	689.3	3a	Syn
89	Melt	SUBO-89-I	—	—	564	545	569	517	—	—	—	2.68	1.71	447.2	4	Syn
89	Melt	SUBO-89-II	—	—	577	—	577	312	—	—	—	—	—	419.9	3a	Syn
90	Melt	SUBO-90	—	—	571	542	572	507	—	1.22	1.00	2.35	1.71	436.6	4	Syn
91	Clast	SUBO-91	−149	—	568	—	549	272	—	1.28	—	1.61	—	63.0	3b-R	Syn-Red
92	Melt	SUBO-92-I	—	—	579	—	586	425	—	—	—	—	—	548.6	3a	Syn

TABLE 4. *Continued.* Parameters obtained from κ–T measurements used in this study.

Depth [m]	Lith.	Sample	Tv1	Tv2	TcH 1	TcH 2	TcC 1	TcC 2	TcC 3	TvPR1	TvPR2	HPR1	HPR2	A40 [%]	Type	Classification
92	Melt	SUBO-92-II	—	−147	571	—	576	310	—	—	—	—	—	795.0	3a-R	Syn-Alt.
93	Melt	SUBO-93	—	—	572	—	575	384	—	—	—	—	—	1596.6	3a-R	Syn-Alt.
95	Melt	SUBO-95-II	—	—	619	—	633	285	—	—	—	—	—	114.8	3a	Syn
95	Melt	SUBO-95-II	—	—	594	—	622	431	316	—	—	—	—	750.7	3a	Syn
97	Melt	SUBO-97	—	−165	576	—	579	319	—	—	—	—	—	791.3	3a-R	Syn-Red
98	Melt	SUBO-98	—	—	534	—	483	—	—	—	—	—	2.25	1854.5	3a	Syn
NR73																
332	Suevite	NR73-332 S	−159	—	574	—	582	—	—	1.22	—	1.66	1.26	55.2	3b	Syn
376	Suevite	NR73-376 S	−175	—	567	—	573	—	—	1.10	—	1.21	1.14	−0.4	2	Syn
376	M.Suev.	NR73-376 S II	−173	−175	575	—	575	—	—	1.22	1.24	1.09	1.10	−0.9	2	Syn
475	Suevite	NR73-475 S	−168	—	575	—	578	—	—	1.10	—	1.63	1.27	17.3	3b-O	Syn + Ox
475	Suevite	NR73-475 S II	−169	−166	574	—	581	—	—	1.10	1.19	1.44	1.23	16.4	3b-O	Syn + Ox
498	S + Gneiss	NR73-498 SG	−174	—	578	–	582	—	—	1.09	–	1.56	1.29	17.7	3b-O	Syn + Ox
498	S + Gneiss	NR73-498 SG II	−152	−170	586	—	551	326	—	1.24	1.02	—	1.88	286.2	3b-R	Syn-Red
528	Gneiss	NR73-528 Gn	−160	−157	590	—	597	—	—	1.35	1.27	1.34	1.21	−24.1	3a	Pre
529	Gneiss	NR73-529 Gn	−157	−165	587	—	592	—	—	1.32	1.37	1.14	1.21	−21.2	3a	Pre
530	Amph.	NR73-530 A	—	—	—	—	586	—	—	—	—	—	—	277.8	1b	Pm + Ox
530	Gneiss	NR73-530 Gn	−158	—	578	—	579	—	—	1.32	—	1.21	1.19	20.8	3a	Pre
530	Gneiss	NR73-530 Gn-II	−156	−163	587	—	589	—	—	1.58	1.34	1.15	1.24	−12.0	3a	Pre
534	Gneiss	NR73-534 Gn	−158	−149	608	—	600	—	—	1.99	1.26	1.22	1.14	11.1	3a	Pre
535	Gneiss	NR73-535 Gn-Wht	−161	−166	580	—	579	—	—	1.22	1.26	1.09	1.16	−12.0	3a	Pre
535	Gneiss	NR73-535 Gn-Blk	−160	−170	576	—	577	—	—	1.24	1.26	1.10	1.18	−11.7	3a	Pre
536	Gneiss	NR73-536 Gn	−165	−170	578	—	588	—	—	1.30	1.35	1.11	1.25	−16.9	3a	Pre
539	Gneiss	NR73-539 Gn	−155	−157	592	—	599	—	—	1.71	1.18	1.15	1.20	4.7	2	Pre
540	Gneiss	NR73-540 SG	−157	−160	578	—	581	—	—	1.28	1.24	1.07	1.07	−19.4	3a	Pre
540	Suevite	NR73-540 SG	−159	−162	579	—	584	—	—	1.30	1.31	1.07	1.18	−26.8	3a	Syn
546	S+Gneiss	NR73-546 SG	−158	—	575	—	580	328	—	1.34	—	1.28	—	172.1	3a-R	Pre + Red
552	S + Gneiss	NR73-552 SG	−147	−153	585	—	591	—	—	1.85	2.97	1.12	1.18	−19.4	3a	Pre
557	Gneiss	NR73-557 Gn	−157	−162	585	—	592	—	—	1.34	1.37	—	1.28	−22.6	3a	Pre
573	Gneiss	NR73-573 Gn	−160	−162	578	—	590	—	—	1.34	1.33	1.18	1.21	−11.5	3a	Pre
574	Gneiss	NR73-574 Gn	−155	−154	583	—	586	—	—	1.48	1.38	1.23	1.66	2.6	2	Pre
612	Gneiss	NR73-612 Gn	−151	−156	590	—	594	—	—	1.42	1.32	—	1.29	−26.9	3a	Pre
617	Amph.	NR73-617 A	—	—	—	—	555	—	—	—	—	—	1.51	665.3	1b	Pm + Ox
621	Gneiss	NR73-621 Gn	−158	−161	580	—	593	—	—	1.38	1.35	1.12	1.15	1.0	2	Pre
623	Gneiss	NR73-623 Gn	−158	−147	582	—	591	—	—	1.49	1.43	1.18	1.16	−1.7	2	Pre
624	Gneiss	NR73-624 Gn	—	—	—	—	—	—	—	—	—	—	—	—	1a	Pm
629	Gneiss	NR73-629 Gn	—	—	—	—	—	—	—	—	—	—	—	—	1a	Pm
630	Gneiss	NR73-630a Gn	−159	−163	579	—	581	—	—	1.34	1.26	1.31	1.24	22.6	3a	Pre

TABLE 4. *Continued.* Parameters obtained from κ–T measurements used in this study.

Depth [m]	Lith.	Sample	Tv1	Tv2	TcH 1	TcH 2	TcC 1	TcC 2	TcC 3	TvPR1	TvPR2	HPR1	HPR2	A40 [%]	Type	Classification
630	Gneiss	NR73-630b Gn	−160	—	579	—	583.90	—	—	—	—	1.09	1.22	−29.4	3a	Pre
664	Gneiss	NR73-664 Gn	−159	—	584	—	593.50	—	—	1.24	—	1.16	1.16	−9.1	3a	Pre
672	Gneiss	NR73-672 Gn	−156	−157	604	—	593.80	—	—	1.58	1.34	1.26	1.13	−9.7	3a	Pre
680	S + Clast	NR73-680 SG	—	−146	554	456	586	440	—	—	0.97	2.02	1.63	51.6	4	Pre + Syn
680	Suevite	NR73-680 S	—	—	—	—	584	489	—	—	—	—	—	198.7	1b	Pm + Ox
820	Metabas.	NR73-820 MB	—	—	—	—	586	349	—	—	—	—	—	390.8	1b	Pm + Ox
821	Metabas.	NR73-821 MB	−180	—	556	—	562	—	—	—	—	1.03	1.10	5.9	2	Pre
826	Metabas.	NR73-826 MB	—	—	—	—	—	—	—	—	—	—	—	—	1a	Pm
827	Metabas.	NR73-827 MB	−165	−161	575	529	571	522	—	1.15	1.21	1.10	1.20	−14.3	4	Pre + Syn
829	Metabas	NR73-829 MB	−155	−162	579	519	578	526	—	1.25	1.20	1.10	1.26	−14.1	4	Pre + Syn

Abbreviations: A40[%], alteration index at 40°C; Depth (m), depth below the surface; HPR, Hopkinson peak ratio; Lith., lithology; Ox, oxidizing; PM, paramagnetic; Red, reducing, refer to text for details on type and classification; T_cH/T_cC, Curie temperature of heating and cooling cycles, respectively, number after T_cH/T_cC (T_cH1, 2…) refers from highest to lowest Curie temperature; T_v1/T_v2, Verwey transition temperature pre- and post-heating, respectively; T_vP, Verwey peak ratio.

generally lower than in pure magnetite, ranging from ∼−149 to ∼−191°C, in agreement with a wide range of generally high cation substitution rates. The Verwey transition is suppressed in the melt region.

From type 1 ($n = 6$), two samples show "1a" characteristics, one of them shows the formation of pyrrhotite during the experiment (1a-R, Table 4), while the remaining paramagnetic samples are type 1b. In SUBO, hydrothermal alteration is prevalent, with only 11 unaltered samples. The most prevalent alteration is reducing, with subtype "R" samples ($n = 18$) widespread through the core. Subtype "O" ($n = 2$) is only observed in a transitory region with both melt and basement clasts present.

DISCUSSION

Magnetic Mineralogy

We performed a magnetic mineralogy study of basement and impact rocks from the inner ring and megablock zone of the Ries crater using surface and drill core samples. Our study confirms that (Ti-)magnetite is the main ferrimagnetic carrier of the magnetic properties and the paleomagnetic directions as described in Pohl (1965), Pohl and Angenheister (1969), Pohl et al. (1977, 2010), and Arp et al. (2019). However, it also shows that the magnetic mineralogy is more complex, and magnetization is often carried by multiple coexisting phases, related to shocked and new formed magnetite. In this section, we will discuss the evolution of the magnetic mineralogy in relation to pre- and syn-impact events. We will further discuss how post-impact hydrothermalism may have played a role in the observed magnetic characteristics. These details have not been studied before, and might be an important aspect to understand the magnetic anomaly pattern.

To this end, we calculated an estimated percentage of magnetic contribution and hydrothermal overprint for each sample location (Figure 8). We used our κ–T data to classify each of our samples into pre- and syn-impact formed magnetite, and divided samples with signs of hydrothermal alteration into those with a more "oxidizing" or "reducing" character. For example, out of 41 κ–T measurements in NR73 (Table 4), seven are paramagnetic. Thus, paramagnetic samples make up 17% of the contribution in NR73. All type 1 samples were excluded from ferrimagnetic contribution calculations.

Magnetic Contribution

Pre-impact magnetite is only found in the basement of NR73 or in the basement clasts in the suevite. These grains are large, originally MD magnetite, which were

exposed to a shock pressure of ~25 GPa (Engelhardt & Graup, 1977), causing grain fracturing, fragmentation, and crystal lattice defects. All type 2, 3, and 4 *basement* samples of NR73 show shock features under the microscope and we consider them as pre-impact magnetite (see Figure 6e,f). Despite the abundance of large magnetite grains, the shocked samples are generally demagnetized (Table 1 and Figure 3) and have lower κ than predicted by empirical calculations (see Tarling & Hrouda, 1993; Table 1, Figures 3 and 6e,f). The magnetite shows intermediate PSD coercivities (~40 mT on average), despite their large grain sizes (>100 μm), which would be expected to imply more MD behavior. The finer end of MD state is suggested for grain sizes of ~10 μm (Nagy et al., 2019), but PSD behavior may still occur up to ~100 μm, under certain lattice strain or anisotropy conditions (see Heider et al., 1996). In NR73, 25 out of 41 samples show these characteristics, leading to a 61% pre-impact contribution (17% paramagnetic; Figure 8).

Syn-impact magnetite formed during or directly related to the impact event from impact melt, and occurs in glass-bearing breccia (suevite). These impactite-formed magnetite grains are generally smaller and thus have higher coercivities (~68 mT) than the shocked ones (see e.g., Figure 6d compared with Figure 6e,f), even after shock deformation (~40 mT). κ and NRM are also generally higher in the syn-impact magnetite (Figure 3, Table 1). Syn-impact magnetite comprises type 2 and 3 curves from Altenbürg and Polsingen, as well as in the NR73 *suevites* (9/41; in total 22%). In SUBO, all samples are classified as syn-impact (83%) with the exception of the paramagnetic type 1 samples (17%; Figure 8).

Hydrothermal Conditions

Subtypes O and R can be classified as pre- or syn-impact with hydrothermal overprint of an already existing ferrimagnetic phase. This overprint is related either to the oxidation of the original phase (subtype O) or to the presence of hydrothermally deposited pyrite which transforms into pyrrhotite during the heating experiment in an argon atmosphere (subtype R).

Type 1 samples were excluded from the magnetic contribution analysis; however, type 1b samples, which indicate the transformation of Fe-carbonate into a ferrimagnetic phase during experiments, require oxidizing conditions for Fe-carbonate deposition. Therefore, we considered samples 1b along with subtype "O", to characterize the oxidizing hydrothermal overprint. This type of overprint is rare in both NR73 (18%) and SUBO (16%; Figure 8), but is prominent in the surface samples (Wengenhausen, type 1b; Altenbürg and Polsingen, type 3-O).

On the other hand, subtype "R" is characterized by the formation of pyrrhotite during the heating experiment and demonstrate the presence of sulfur-rich minerals like pyrite. The formation of pyrite indicates a reducing nature of the hydrothermal fluids (Osinski, 2005). This is the most dominant hydrothermal overprint in SUBO (51%), but rare in NR73 (only 5%).

Samples that do not meet the 1b, "O," or "R" characterization are proposed as hydrothermally unaltered samples that did not exhibit significant magnetic overprint or a hydrothermal effect in their magnetic properties. This is the vast majority of NR73 (76%) and one third of the samples of SUBO (32%), mostly in the continuous melt section (Table 4).

A Conceptual Model of Magnetic Evolution

Pre-impact

Our results provide the first in-detail characterization of the magnetic mineralogy in the shocked basement of the Ries crater. Before the impact, the regional magnetization was carried mostly by pure magnetite with low rates of oxidation (maximum calculated vacancies around 0.05 for 3 cations, Table 3) and large grain sizes (up to ~200 μm) suggesting an initial MD state (Heider et al., 1996; Nagy et al., 2019). From the size and abundance of these grains in thin sections, we estimate a concentration of ~1% magnetite in the bulk gneiss samples. At this concentration, we suggest that the original κ in the pre-impact Variscan gneisses range between 10^{-2} and 10^{-1} SI (see Tarling & Hrouda, 1993). This estimate is in line with regional trends. Studies from (not shocked) Variscan granitoid basement rocks, such as the Vosges mountains in France, show κ values ranging from 10^{-3} SI to ~10^{-1} SI (Edel et al., 2013). In fresh, hydrothermally unaltered granite samples from the Soultz-sous-Forêts granitoid, κ values are around 10^{-2} SI (Just & Kontny, 2011), and a borehole of the German Continental Deep Drilling Programme (KTB) into the Variscan basement in the Oberpfalz region (Bavaria, Germany) shows κ of (not shocked) gneisses and metabasites in the same range of 10^{-3} to 10^{-1} SI (Berckhemer et al., 1997).

At impact, the shockwave alters the magnetic properties of magnetite in three distinct and independent ways: κ reduction (e.g., Kumar et al., 2023; Reznik et al., 2016), demagnetization (e.g., Gilder et al., 2006), and SRM acquisition (e.g., Gattacceca et al., 2006, 2007; Sato et al., 2021). These three effects will irreversibly affect the total magnetization values observed in Table 1, so we must address them individually.

The shock-induced grain fracturing (see Figure 6e,f) and crystal lattice defect formation may reduce κ in

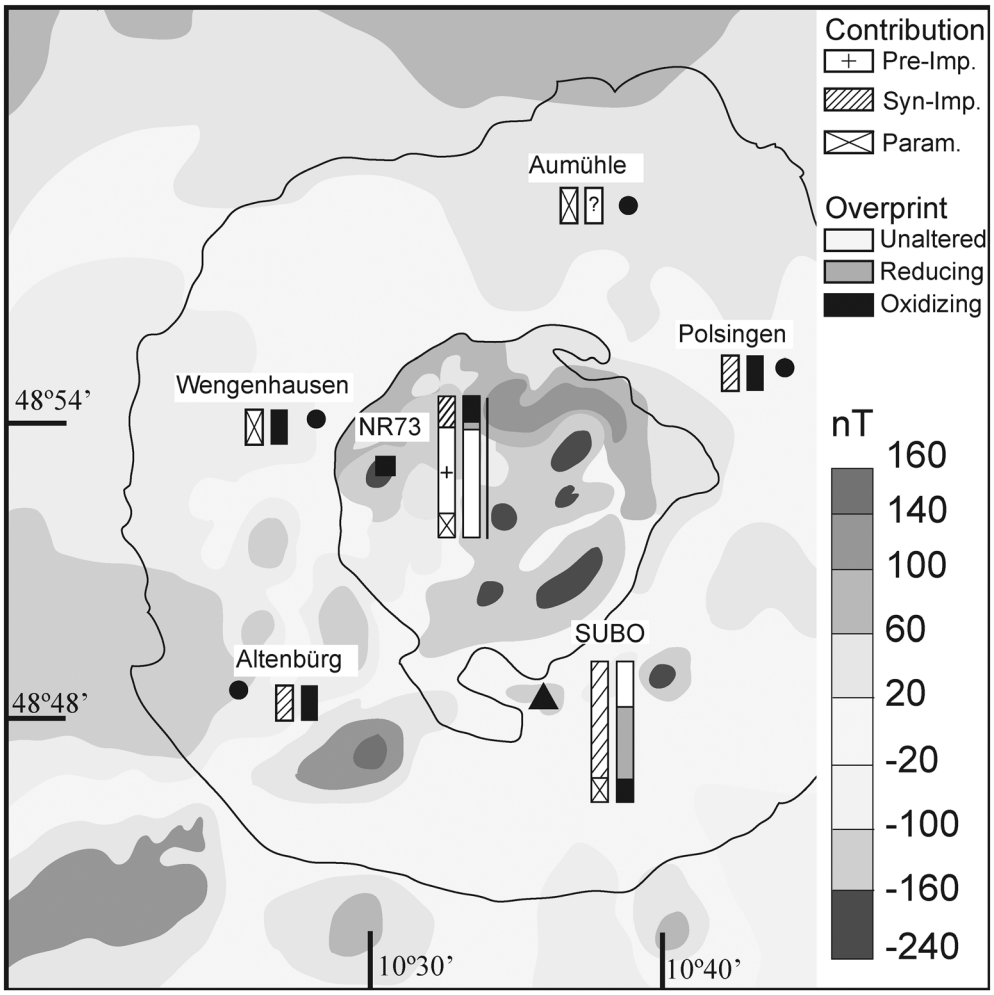

FIGURE 8. Aeromagnetic anomaly map (nT) (after Pohl et al., 2010), with sampling locations. Vertical bars represent the calculated (%) of magnetic contribution (pre-, syn-, or paramagnetic) and hydrothermal overprint conditions. Refer to text for details in calculations of percentages.

magnetite by up to 90% after shock pressures of 5 GPa (the Hugoniot elastic limit of magnetite, Ahrens & Johnson, 1995; Reznik et al., 2016). Shock deformation causes grain size reduction and associated (apparent or real) domain state decrease, through increased domain wall-pinning (Lindquist et al., 2015; Mendes & Kontny, 2024; Reznik et al., 2016). As the basement (expected original κ $\sim 10^{-2}$ to 10^{-1} SI) was exposed to $\sim$25 GPa, we attribute its reduced κ (observed $\sim 10^{-4}$ SI, Table 1, Figure 3) and relatively high coercivities ($\sim$40 mT, consistent with PSD behavior; Table 2; Figures 4 and 5) to shock deformation.

NRM intensities in the Ries basement are generally quite low (<0.1 A m^{-1} Figure 3, Table 1) than in the intact Variscan basement (e.g., KTB drill cores show NRM intensities around ~ 0.1 A m^{-1}, locally up to 10 A m^{-1}; Berckhemer et al., 1997). At impact, the demagnetization of the target and SRM acquisition occur simultaneously but independently (Gattacceca et al., 2010). It is widely accepted that ferrimagnetic minerals are subject to substantial demagnetization through compression, even at pressures well below 5 GPa (e.g., Louzada et al., 2011). The demagnetization of an existing NRM strongly depends on the coercivity of the target and thus, indirectly, the grain size (e.g., Cisowski & Fuller, 1978). Shock demagnetization is stronger in the low coercivity fraction of the NRM (MD magnetite, Bezaeva et al., 2007, 2010; Gattacceca et al., 2010; Jackson et al., 1993; Louzada et al., 2007; Pearce & Karson, 1981). In fact, Kletetschka et al. (2004) demonstrated that <2 GPa MD magnetite may lose up to $\sim$90% of its pre-shock NRM, compared to a loss of $\sim$70% in SD magnetite. In (Ti-)magnetite, the demagnetization is also correlated to the Ti content (Bezaeva et al., 2010); however, our pre-impact magnetite is mostly pure (Table 3), so this is not a factor to consider

in our case. MD magnetite is also particularly susceptible to SRM acquisition (e.g., Tikoo et al., 2015). Compression at low pressures in the presence of an ambient field may allow for SRM acquisition (Fuller, 1977; Gattacceca et al., 2007, 2010; Louzada et al., 2011; Srnka et al., 1979). Although the acquisition of SRM depends on magnetic mineralogy and grain size (e.g., Sato et al., 2021), it is less efficient and intensities are several times lower than the original NRM acquired through other processes, for example, TRM (Gattacceca et al., 2006). Therefore, we attribute the decreased NRM intensities of our rocks to shock demagnetization, and rather neglect an SRM contribution to the total magnetization of these rocks. The existing literature for the paleomagnetic directions in the shocked basement of NR73 (Pohl, 1977) suggests scattered inclinations, which implies that no primary pre-impact magnetization was retained, and no stable post-impact remagnetization was acquired. Due to the reduced intensities, the dominance of induced magnetization ($Q < 1$), and likely scatter of directions during the modification stage of the crater, the contribution of a potential SRM would be insignificant to the magnetic properties of the basement of the Ries crater.

The shocked Ries basement shows similarities to those observed in the much larger Chicxulub impact crater, Mexico (e.g., Mendes et al., 2023), where shocked magnetite is also the main carrier of magnetization. Magnetite grains with similar sizes (>200 μm) exhibit PSD state with coercivities around ~40 mT and a strongly reduced κ (Mendes et al., 2023). The κ (~10^{-5} to 10^{-4} SI) and NRM (~0.01 A m^{-1}; Mendes et al., 2023) of the shocked basement in Chicxulub are comparable to the κ and NRM observed here. In Chicxulub, the negative magnetic anomaly along the peak-ring is associated with this shocked magnetite (Mendes et al., 2023). The peak-ring structure in Chicxulub consists of a kilometer-thick section of uplifted basement morphologically similar to the inner ring in Ries (see Figure 1c), where reduced κ and NRM cause a local drop in total magnetization along the structure, creating the negative magnetic anomaly (Mendes et al., 2023). Due to the preponderance of literature on the systematic reduction of κ and NRM due to shock as described above, we consider the influence of demagnetized basement for negative magnetic anomalies over impact craters to be a universal observation and should be carefully weighed in magnetic anomaly interpretations of these structures.

Syn-Impact

At the time of impact and the minutes immediately after, the high emplacement temperatures of the suevite and impact melt (up to 900°C in the suevite and >2000°C for the impact melt, Osinski et al., 2004) allowed for the formation of new and thus intact cation-substituted magnetite. The main characteristic of this phase is mostly a low cation substitution, with Curie temperatures ~570°C (Tables 3 and 4), indicating compositions close to pure magnetite. Some minor cation-substituted magnetite with lower Curie temperatures (~540°C) were also observed in the impact melts of SUBO. All newly formed magnetite phases show Q-ratios >1, indicating that magnetization is mainly controlled by NRM (Figure 3a,c).

The κ, NRM intensity and domain state of magnetite in suevite (NR73 and Altenbürg), and impact melt (SUBO and Polsingen) varies strongly, and thus we will discuss them separately. The surface suevite from Wengenhausen and Aumühle show a strong hydrothermal overprint, so we will discuss them in detail under the next heading.

In NR73, magnetite in *suevite* has higher κ and NRM intensity than in shocked basement (Table 2) and the suevite shows a wide range of domain states and coercivities, extending from SD to MD (Figure 4). This range show either that larger shocked magnetite grains inherited from the basement clasts contribute to the total grain population or that different cooling rates during magnetite crystallization from impact melt caused a range of grain sizes.

In Altenbürg, κ and NRM values are very low, and magnetite shows a low cation substitution (Table 3). The small grains, with skeletal textures in isolated clusters (Figure 6), suggest that the cooling of this surface suevite was faster than in the crater suevite, which may have not allowed for a more prolific magnetite crystallization. Furthermore, the cation deficiency in this sample (vacancies = 0.1; Table 2) and type 3b-O κ–T curves suggests some degree of maghemitization and oxidation. This maghemite seems to be transformed into magnetite during the κ–T experiment, causing a positive A40 of ~47%, and the appearance of the Verwey transition in a second low-temperature run (Table 2). The Verwey transition may have been repressed in the first LT curve by the maghemitization, since it is sensitive to oxidation (Aragón et al., 1985). We consider the low concentration of magnetite, its small grain sizes, and its oxidation/maghemitization to be the cause of the low magnetization in Altenbürg.

The long exposure to high temperatures after the impact event is also expected to have strong effects on the shocked pre-impact magnetite. Recent studies of experimentally heated shocked magnetite indicate that thermal annealing of shock-induced lattice defects has a significant effect on the recovery of magnetic properties (Kontny et al., 2018; Mendes et al., 2023; Mendes & Kontny, 2024). With thermal annealing, domain states appear to increase and some κ is restored (Kontny et al., 2018; Mendes & Kontny, 2024). This κ restoration

after heating is evident in notoriously irreversible κ–T curves with positive A40[%] values of 20%–50% (e.g., see fig. 1 in Kontny et al., 2018). Shocked basement shows irreversible type 3 κ–T curves, however with negative A40 [%]. Negative values indicate a transformation of magnetite to a less magnetic phase, such as ilmenite (Hrouda, 2003; Table 4). These negative values do not exclude annealing as a process, but may suggest that κ increase through annealing could be masked by a larger κ decrease from mineral transformation. An example for the transformations of hematite to magnetite during heating in argon atmosphere in natural samples of Chicxulub showcases how mineral transformations dominate and overprint the signal of thermal magnetite annealing, although annealing still takes place (Mendes et al., 2023; Mendes & Kontny, 2024). Under these circumstances, thermal annealing is only identified through very sensitive methods that identify small domain state variations, such as first order reversal curve diagrams (Mendes & Kontny, 2024).

The presence of type 2 curves in the shocked basement suggests that not all basement magnetite undergoes mineral transformations and also do not experience an annealing-induced κ increase during the experiment. Therefore, we propose that these samples may have already been annealed naturally by the emplacement of suevite dykes (>900°C) that intersect the basement. Immediately after emplacement, contact with the suevite could lead to high enough temperatures to anneal the physical defects, without necessarily creating favorable chemical conditions for mineral transformations. In the absence of mineral transformations, magnetite shocked above 5 GPa always shows an increase in κ after heating (Kontny et al., 2018; Mendes & Kontny, 2024). The absence of a κ increase necessitates that either: (1) samples already experienced annealing in nature or (2) the shock pressures in the basement are heterogeneous, and did not reach 5 GPa in NR73, leading to irreversible brittle deformation (fracturing and fragmentation) but no plastic deformation that can be reverted by thermal annealing. However, we find explanation (2) unlikely for the basement of NR73, where shock pressures at the sampled depths (~600 m; Figure 2) are estimated to be around 25 GPa (Engelhardt & Graup, 1977). Some shock attenuation is identified in the basement; however, the shock pressures are described to be still above 5 GPa until around 1200 m depth (Engelhardt & Graup, 1977). Furthermore, the intensity of grain fracturing and fragmentation of the magnetite (Figure 6e,f), low NRM, κ (Table 1, Figure 3), and the apparently decreased PSD domain state (Table 2, Figure 4) strongly suggests that the magnetite was exposed to shock pressures above the 5 GPa threshold. Thus, we favor the interpretation that an abundance of suevite dyke intercalations within the basement leads to a natural annealing of the magnetite immediately after the impact event. It is possible that the intensity of the irreversible brittle deformation is significantly more extensive over plastic reversible deformation, thus making the restoration of magnetic properties through annealing insignificant at the larger scale.

Impact melts in SUBO and Polsingen have low κ and NRM intensity (Table 1; Figure 3), with general small apparent magnetite grain size, decreased domain state, and associated high coercivity (Table 2; Figure 4, Figure 6i,j). In SUBO, magnetite is slightly more cation-substituted than in the other suevite, with T_c on average at around 570°C in the main phase, and 540°C for minor phases (Table 4). Coercivity values of ~68 mT of the magnetite phase suggest a SD/fine-PSD domain state (Figures 4 and 5, Table 2), consistent with grain sizes that can be too small for EPMA (with some exceptions, see Figure 6h). Our results are in contrast to previously published data of SUBO (Pohl et al., 2010) that described NRM intensity up to 1.5 A m^{-1}, whereas our samples are on average ~0.13 A m^{-1}. We attribute the low magnetization to the prevalence of very small SD grains and cation-substituted magnetite in the impact melt, as well as the presence of ilmenohematite which gives these samples their characteristic red color (Osinski et al., 2004, 2005). Low intensities can also be caused by cation-substituted hematite with contribution to the NRM signal ubiquitous in the melt, but rare in in the suevite (Table 2). We attribute the deviation between our results and the results published by Pohl et al. (2010) to natural heterogeneity, with high intensities being outliers to the average. In the Polsingen red suevite, we observed a lower cation-substitution (T_c ~577°C) and mean coercivity of ~40 mT (Table 2; Figures 4 and 5a), suggesting not only coarser grains but also PSD state. PSD state behavior is retained until around ~10 µm (Nagy et al., 2019), but grains of that size are rare in the impact melt (note that Figure 6 depicts the only grain used for EPMA in Figure 6h,i). As in SUBO, the small (~5 µm) magnetite and (cation-substituted) hematite (Figure 5, Table 2) also explains the low NRM intensities.

Post-Impact Hydrothermal Overprint

The post-impact hydrothermal system in the Ries crater was well developed, but generally of low temperature (~130 to 300°C, Osinski, 2005) and not very laterally extensive (Sapers et al., 2017). The hydrothermal alteration affects each of the magnetic phases, and the main characteristics of the hydrothermal alteration are overall similar in NR73 and SUBO. Surface samples from the megablock zone are limited to a first, high-temperature phase (see below).

In *pre-impact* minerals from the basement and in clasts found in suevite of SUBO, hydrothermal alteration causes minor oxidation of pure magnetite likely along free surfaces of the fractures and grain boundaries (Figure 8). The hydrothermal fluids are also responsible for the deposition of Fe-carbonates responsible for type 1b curves (Table 4, Figure 8). In some pre-impact samples, IRM modeling suggests the presence of some hematite, which we interpret as likely formed from this same hydrothermal phase. The hydrothermal systems described in the Ries impact crater (Newsom et al., 1986; Osinski, 2004, 2005; Osinski et al., 2013; Sapers et al., 2017) have generally low temperatures, around ~130 to 300°C in a first, steam-dominated phase, and <100°C during a second, long-lasting phase (Osinski, 2005). These temperatures are too low to cause annealing in pre-impact magnetite, with minimum required temperatures ~45–540°C (Mendes et al., 2023; Mendes & Kontny, 2024). It is worth noting that despite 76% of the ferrimagnetic samples of NR73 being hydrothermally "unaltered", some secondary ilmenite is observed in the cracks of the shocked magnetite (Figure 6e), denoting that hydrothermal alteration happened, but did not overprint or affect strongly the magnetic characteristics in the Ries basement. In NR73, 18% of the samples show oxidizing and only 5% reducing conditions, with most of the alteration localized in the suevites (Table 4). Thus, despite ubiquitous hydrothermal alteration in NR73, the magnetic phases were generally preserved.

In *syn-impact* magnetite, the hydrothermal overprint also varies regionally. The paramagnetic type 1a curves from Aumühle were taken from degassing channels, where a large amount of secondary ilmenite is deposited (see EPMA data in File S4, Figure 6c). In Wengenhausen and the upper suevite of SUBO (Table 4), type 1b curves suggest the presence of some Fe-carbonates in the sample, which transform into a ferrimagnetic phase during κ–T experiments, likely (Ti-)maghemite or (Ti-) magnetite. Suevite from NR73 and Altenbürg also shows mostly oxidizing hydrothermal alteration and maghemitization (Table 4, Figure 8).

In contrast to NR73, a hydrothermal overprint in SUBO is dominant, with 64% of the samples showing signs of overprint. The majority of the overprint occurring in SUBO is reducing (51% of the samples; Figure 8; Table 4), with a majority of samples showing the formation of pyrrhotite during the heating experiment. Pyrrhotite is formed from paramagnetic pyrite, deposited in a reducing environment. It is worth noting that in SUBO, at least one sample shows the presence of both Fe-carbonates and pyrite (see Table 4 sample SB-33). These results suggest that both alteration conditions affected the samples, possibly requiring continued evolution of the hydrothermal fluids over time.

To our knowledge, this is the first study focusing on the influence of hydrothermalism on magnetic mineralogy. Our results agree well with previously published studies regarding the hydrothermal systems more generally, suggesting that most of the alteration is localized in the suevites (e.g., Osinski et al., 2013). A two-stage cooling model has been proposed in literature (e.g., Naumov, 2005; Sapers et al., 2017) that describes a first, rapid convection-driven cooling above boiling temperatures through steam and degassing, and a second long-lasting gradual cooling stage. The samples from Aumühle which were taken from degassing pipes have been attributed to this first stage (Chao, 1978; Newsom et al., 1986; Sapers et al., 2017). We suggest the first stage is responsible for generally reducing conditions, leading to the deposition of the Fe-sulfides in the inner crater suevite. We propose that in the basement, the injection of suevite dykes during the formation of the crater (Stöffler, 1977; Stöffler & Grieve, 2007) and partial melting of the gneiss and metabasite created a very Ti-rich impact melt and fluids at the time of impact. Although vapor convection-driven alteration of the first stage is restricted to the upper suevites, we believe that the high-temperature suevite dykes in the basement have also created conditions that allow for the contemporaneous deposition of the secondary ilmenite observed in the fractures of the shocked magnetite throughout the basement.

The second hydrothermal phase (see Sapers et al., 2017) likely lasted for a long time (up to 250 kyr), and was characterized by slow cooling of heated material (e.g., Osinski et al., 2013) and weakly alkaline (pH >8–9) fluids, which are derived from meteoritic water and from the crater lake (Muttik et al., 2011). These alkaline fluids may be responsible for the creation of oxidizing conditions for the formation of the Fe-carbonates, maghemitization, and local oxidation of pyrite to goethite in the surface samples and suevite of NR73 and SUBO. The second stage is stronger in the inner crater, and we suggest that it may locally overprint the first stage through oxidation of the earlier formed pyrite, as subtype "R" is absent in NR73. Alternatively, it is also possible that first-stage pyrite only forms where enough Fe and S species are available in the fluid. The high carbon content within claystone, such as those from the Mesozoic sedimentary cover (Graup, 1975), could lead to more reducing fluids locally, which enhances the mobility of Fe and S species. While in the inner crater no sedimentary cover is preserved in the crater basement (see Figure 2), it is hypothetically possible that some of the sequence may be preserved closer to the inner ring. Both the second-stage oxidation of pyrite or the absence of pyrite deposition can reasonably explain the absence of subtype "R" in NR73.

Implications for the Magnetic Anomaly Pattern

Magnetic anomalies in the Ries crater have long been related to the presence of a strong NRM reverse polarity in the crater suevite (Arp et al., 2019; Iseri et al., 1989; Pohl, 1965; Pohl & Angenheister, 1969; Pohl et al., 1977, 2010). Our results from NR73 corroborate this hypothesis, as the Q-ratios show that the magnetization of the suevite is controlled by the NRM, and a strong total magnetization ($\sim$2 A m^{-1}). In contrast, the total magnetization of the basement is much weaker (average $\sim$0.1 A m^{-1}), and the induced magnetization is dominant over the NRM ($Q < 1$). With κ reduced by up to two orders of magnitude ($\sim 10^{-4}$ from originally estimated $\sim 10^{-2}$ SI), the magnetization in the basement is very low ($\sim$0.1 A m^{-1}, Table 1). This allows the thick layer ($\sim$200 m) of strongly reverse polarity suevite to dominate the magnetic signal and create the negative magnetic anomalies in the inner crater.

In SUBO, this relationship is not so clearly developed. Although the Q-ratio is >1, the total magnetization in the investigated samples is generally one order of magnitude lower than in NR73 (average $\sim$0.14 A m^{-1}, Table 1). SUBO, which was drilled into the uplifted inner ring (see Figure 1 and Arp et al., 2019), did not reach the basement; however, the modeling of the magnetic anomaly performed by Pohl et al. (2010) estimates that the basement is only $\sim$120 m below the surface. This means that the impactite layer of $\sim$100 m, which is only slightly stronger magnetized than the demagnetized basement (Table 3), has only half the thickness of the NR73 impactites. However, the intensity of the negative anomaly is comparable to NR73 (see Figure 1d, and Pohl et al., 2010). The NRM of the suevite is very weak (average $\sim$0.01 A m^{-1}), and the melt, albeit stronger ($\sim$0.16 A m^{-1}), presents only a very thin (at most $\sim$50 m) continuous layer, which is still two orders of magnitude weaker than the impactites layer of NR73. The weakness of the impactites, combined with the thicker and high-uplifted demagnetized basement, lead us to propose that in SUBO the reverse polarity of NRM may not be the dominant reason for the negative anomaly as previously proposed by Pohl et al. (2010), but rather is caused by the overall lack of magnetization instead. While NRM and κ can be locally strong (see Figure 2 and Pohl et al., 2010), these are outliers rather than a lithology wide trend. The absence of magnetization creates a contrast with the background magnetization, which causes the anomaly. This hypothesis can be tested by modeling the anomaly; however, combining the results presented by Pohl et al. (2010) and in our study, such modeling is beyond the scope of the present work.

A significant contribution from the uplifted demagnetized basement would be in agreement with observations from the Chicxulub impact structure (Mexico, Mendes et al., 2023), where a layer of shocked, demagnetized basement in the uplifted peak-ring created a region of low total magnetization ($\kappa = \sim 1 \times 10^{-3}$ SI; NRM = $\sim$0.01 A m^{-1}). Syn-impact cation-substituted magnetite in the impact melt of the peak-ring shows much stronger NRM (up to 1 A m^{-1}), κ (up to 20×10^{-3} SI), Q-ratios >1, and reverse polarity inclinations (Inc. = $\sim -44°$; see Kring et al., 2020; Mendes et al., 2023; Tikoo et al., 2017). Despite the reverse polarity in the peak-ring, the newly formed magnetite from the melt is suggested to cause the positive magnetic anomaly in the adjacent melt pool in the central basin of the crater (e.g., Rebolledo-Vieyra et al., 2010; Urrutia-Fucugauchi et al., 2011). However, the relationship between the magnetic mineralogy and the positive anomaly is still under debate, as no drilling has recovered material from this melt pool until now. Nonetheless, the inclination found in the melt layer of the peak-ring agrees with the expected direction for the time of impact at Chron 29r, which lasted for at least 250 ka after the impact (Sprain et al., 2018). This observation raises a question regarding the origin of the magnetic anomaly: if the central basin cooled below 580°C within 250 ka (which is likely) and shows the same reverse inclination as the rest of the melt, why does it present such a strong positive magnetic anomaly? This is different to the observation in the Ries crater made in this paper and in previous studies (Arp et al., 2019; Pohl, 1965; Pohl & Angenheister, 1969; Pohl et al., 1977, 2010), which considers the direction and intensity of the NRM to be the main controlling factor for the magnetic anomalies. A comparison between Ries and Chicxulub highlights how the understanding of the relationship between magnetic mineralogy, impact processes, and magnetic anomalies over craters remains a challenge in impact research. We suggest that the contribution of the demagnetized basement to the magnetic anomaly is generally underestimated, and often overlooked.

CONCLUSIONS

We have investigated the magnetic properties and magnetic mineralogy in suevite, impact melt, and shocked basement from the surface (outer ring and megablock zone), and from boreholes NR73 (inner crater) and SUBO (inner ring) in the Nördlinger Ries impact crater, Germany. We discriminated pre-, syn-, and post-impact processes to better understand the evolution of crater magnetism, and the contribution for the total magnetization and magnetic anomaly pattern.

The main magnetic mineral in the surface and NR73 suevite is low cation-substituted magnetite. This phase is also observed in SUBO, but a second, more cation-substituted magnetite also contributes to the magnetization. Suevites in NR73 have a strong total

magnetization (~2 A m^{-1}), whereas in SUBO both melt and suevite show much lower magnetizations (~0.14 A m^{-1}). We attribute the lower magnetization to the smaller grain sizes and related domain states, higher cation-substitution, and an overall higher concentration of ilmenohematite rather than magnetite, in these rocks.

The shocked basement of NR73 contains pure, shocked, and demagnetized magnetite (~0.1 A m^{-1}), with PSD domain state and high coercivity, despite large grain sizes (~200 μm). The shocked magnetite was likely annealed locally, in contact with high-temperature suevite and impact melt (900–2000°C).

A two-stage hydrothermal system altered but did not significantly overprint the preexisting magnetic properties of our sampled lithologies. A first, steam-driven fluid is responsible for the widespread formation of Fe-sulfides and ilmenite locally in the shocked basement. This was followed by a weakly alkaline longer lasting system, depositing Fe-carbonates, and oxidizing existing phases.

We propose that the negative magnetic anomalies above NR73 and SUBO have different origins. In NR73, it is caused by a strong reverse polarity NRM, in accordance with previously published literature. However, for the local negative magnetic anomaly at SUBO we suggest that the anomaly is caused by an overall absence of magnetization. A thicker section of contiguous uplifted and demagnetized basement overlain by a magnetically weak melt and suevite layer causes a localized lack of magnetization that contrasts with the background magnetization, causing the local magnetic anomaly. This mechanism has been observed before and is proposed to explain negative anomalies over other large impact craters, such as the Chicxulub crater (Mexico). However, a holistic understanding of the relationship between magnetic mineralogy and magnetic anomalies in impact craters remains elusive and requires new modeling of the magnetic anomalies, incorporating the here suggested concept.

Acknowledgments—The authors would like to thank Ksenia Gaus and Ruben Winstel for the assistance in the laboratory and sampling process, and Kirsten Drüppel for discussion on the mineral chemical composition of magnetite. This work was funded by the German Research Foundation, project number 432762445, and partially supported by the National Science Centre (NCN), Poland, in the frame of scientific project no. 2019/03/X/ST10/00139. The authors do not have any conflict of interests to declare. The authors acknowledge the thorough reviews by Michael Poelchau, Amar Agarwal, and Bjarne Almqvist. Open Access funding enabled and organized by Projekt DEAL.

Editorial Handling—Dr. Michael H. Poelchau

REFERENCES

Ahrens, T. J., and Johnson, M. L. 1995. Shock Wave Data for Rocks. In *Rock Physics & Phase Relations*, edited by T. J. Ahrens, 35–44. Washington, DC: American Geophysical Union.

Ames, D. E., Watkinson, D. H., and Parrish, R. R. 1998. Dating of a Regional Hydrothermal System Induced by the 1850 Ma Sudbury Impact Event. *Geology* 26: 447–450.

Aragón, R., Buttrey, D. J., Shepherd, J. P., and Honig, J. M. 1985. Influence of Nonstoichiometry on the Verwey Transition. *Physical Review B* 31: 430–36. https://doi.org/10.1103/PhysRevB.31.430.

Arp, G., Kolepka, C., Simon, K., Karius, V., Nolte, N., and Hansen, B. T. 2013. New Evidence for Persistent Impact-Generated Hydrothermal Activity in the Miocene Ries Impact Structure, Germany. *Meteoritics & Planetary Science* 48: 2491–2516. https://doi.org/10.1111/MAPS.12235.

Arp, G., Reimer, A., Simon, K., Sturm, S., Wilk, J., Kruppa, C., Hecht, L., et al. 2019. The Erbisberg Drilling 2011: Implications for the Structure and Postimpact Evolution of the Inner Ring of the Ries Impact Crater. *Meteoritics & Planetary Science* 54: 2448–82. https://doi.org/10.1111/maps.13293.

Bauberger, W., and Mielke, H. 1974. Petrographiche Profildarstellung Der Forschungsbohrung Nördlingen 1973.

Berckhemer, H., Rauen, A., Winter, H., Kern, H., Kontny, A., Lienert, M., Nover, G., et al. 1997. Petrophysical Properties of the 9-km-Deep Crustal Section at KTB. *Journal of Geophysical Research: Solid Earth* 102: 18337–61. https://doi.org/10.1029/96JB03396.

Bezaeva, N. S., Gattacceca, J., Rochette, P., Sadykov, R. A., and Trukhin, V. I. 2010. Demagnetization of Terrestrial and Extraterrestrial Rocks under Hydrostatic Pressure up to 1.2 GPa. *Physics of the Earth and Planetary Interiors* 179: 7–20. https://doi.org/10.1016/J.PEPI.2010.01.004.

Bezaeva, N. S., Rochette, P., Gattacceca, J., Sadykov, R. A., and Trukhin, V. I. 2007. Pressure Demagnetization of the Martian Crust: Ground Truth from SNC Meteorites. *Geophysical Research Letters* 34: 23202. https://doi.org/10.1029/2007GL031501.

Biaøo, I., Kozøowski, A., Wack, M., Wøodek, A., Gondek, Ł., Kakol, Z., Hochleitner, R., Zywczak, A., Chlan, V., and Gilder, S. A. 2019. The Influence of Strain on the Verwey Transition as a Function of Dopant Concentration: Towards a Geobarometer for Magnetite-Bearing Rocks. *Geophysical Journal International* 219: 148–158. https://doi.org/10.1093/GJI/GGZ274.

Bowles, J. A., Jackson, M. J., Berquó, T. S., Sølheid, P. A., and Gee, J. S. 2013. Inferred Time- and Temperature-Dependent Cation Ordering in Natural Titanomagnetites. *Nature Communications* 4: 1–9. https://doi.org/10.1038/ncomms2938.

Bringemeier, D. 1994. Petrofabric Examination of the Main Suevite of the Otting Quarry, Nördlinger Ries, Germany. *Meteoritics* 29: 417–422. https://doi.org/10.1111/J.1945-5100.1994.TB00607.X.

Carporzen, L., and Gilder, S. A. 2010. Strain Memory of the Verwey Transition. *Journal of Geophysical Research: Solid Earth* 115: 5103. https://doi.org/10.1029/2009JB006813.

Chao, E. C. T. 1978. Principal Exposures of the Ries Meteorite Crater in Southern Germany. *Bayersiches Geologisches Landesamt* 84.

Cisowski, S. M., and Fuller, M. 1978. The Effect of Shock on the Magnetism of Terrestrial Rocks. *Journal of Geophysical Research: Solid Earth* 83: 3441–58. https://doi.org/10.1029/JB083IB07P03441.

Day, R., Fuller, M., and Schmidt, V. A. 1977. Hysteresis Properties of Titanomagnetites: Grain-Size and Compositional Dependence. *Physics of the Earth and Planetary Interiors* 13: 260–67. https://doi.org/10.1016/0031-9201(77)90108-X.

Dunlop, D. J., and Ozdemir, O. 2000. Effect of Grain Size and Domain State on Thermal Demagnetization Tails. *Geophysical Research Letters* 27: 1311–14. https://doi.org/10.1029/1999GL008461.

Dunlop, D. J. 2002. Theory and Application of the Day Plot (Mrs/Ms Versus Hcr/Hc) 1. Theoretical Curves and Tests Using Titanomagnetite Data. *Journal of Geophysical Research: Solid Earth* 107: EPM 4-1. https://doi.org/10.1029/2001JB000486.

Dunlop, D. J. 2014. High-Temperature Susceptibility of Magnetite: A New Pseudo-Single-Domain Effect. *Geophysical Journal International* 199: 707–716. https://doi.org/10.1093/GJI/GGU247.

Edel, J. B., Schulmann, K., Skrzypek, E., and Cocherie, A. 2013. Tectonic Evolution of the European Variscan Belt Constrained by Palaeomagnetic, Structural and Anisotropy of Magnetic Susceptibility Data from the Northern Vosges Magmatic Arc (Eastern France). *Journal of the Geological Society* 170: 785–804. https://doi.org/10.1144/JGS2011-138.

Engelhardt, W. V., and Bertsch, W. 1969. Shock Induced Planar Deformation Structures in Quartz from the Ries Crater, Germany. *Contributions to Mineralogy and Petrology* 20: 203–234. https://doi.org/10.1007/BF00377477/METRICS.

Engelhardt, W. V., and Graup, G. 1977. Stosswellenmetamorphose im Kristallin der Forschungsbohrung Noerdlingen 1973. *Geologica Bavarica* 75: 255–271.

Engelmann, R. 2008. Bestimmung Diagnostischer Magnetischer Übergangstemperaturen von Synthetischen Titanomagnetiten Und Ilmenit-Hämatit-Mischkristallen https://doi.org/10.11588/HEIDOK.00008392.

Fraas, E., and Branco, W. 1901. Das vulcanische Ries bei Nördlingen in seiner Bedeutung für Fragen der allgemeinen. *Geologie*.

Fuller, M. D. 1977. Review of Effects of Shock (<60 kbar; $<6\times10^9$ Pa) on Magnetism of Lunar Samples. *Philosophical Transactions of the Royal Society of London. Series A, Mathematical and Physical Sciences* 285: 409–416. https://doi.org/10.1098/RSTA.1977.0082.

Gattacceca, J., Boustie, M., Lima, E., Weiss, B. P., de Resseguier, T., and Cuq-Lelandais, J. P. 2010. Unraveling the Simultaneous Shock Magnetization and Demagnetization of Rocks. *Physics of the Earth and Planetary Interiors* 182: 42–49. https://doi.org/10.1016/j.pepi.2010.06.009.

Gattacceca, J., Lamali, A., Rochette, P., Boustie, M., and Berthe, L. 2007. The Effects of Explosive-Driven Shocks on the Natural Remanent Magnetization and the Magnetic Properties of Rocks. *Physics of the Earth and Planetary Interiors* 162: 85–98. https://doi.org/10.1016/J.PEPI.2007.03.006.

Gattacceca, J., Boustie, M., Weiss, B. P., Rochette, P., Lima, E. A., Fong, L. E., and Baudenbacher, F. J. 2006. Investigating Impact Demagnetization through Laser Impacts and SQUID Microscopy. *Geology* 34: 333–36. https://doi.org/10.1130/G21898.1.

Gilder, S. A., Le Goff, M., and Chervin, J. C. 2006. Static Stress Demagnetization of Single and Multidomain Magnetite with Implications for Meteorite Impacts. *High Pressure Research* 26: 539–547. https://doi.org/10.1080/08957950601092085.

Graup, G. 1975. Das Kristallin im Nördlinger Ries schnell-Druck Schumacher+ Speh.

Graup, G. 1999. Carbonate-Silicate Liquid Immiscibility upon Impact Melting: Ries Crater, Germany. *Meteoritics & Planetary Science* 34: 425–438. https://doi.org/10.1111/J.1945-5100.1999.TB01351.X.

Grieve, R. A. F. 1999. Some of the Missing Melt Fraction Found? *Meteoritics & Planetary Science* 34: 311–12.

Gulick, S. P. S., Barton, P. J., Christeson, G. L., Morgan, J. V., McDonald, M., Mendoza-Cervantes, K., Pearson, Z. F., et al. 2008. Importance of Pre-Impact Crustal Structure for the Asymmetry of the Chicxulub Impact Crater. *Nature Geoscience* 1: 131–35. https://doi.org/10.1038/ngeo103.

Heider, F., Zitzelsberger, A., and Fabian, K. 1996. Magnetic Susceptibility and Remanent Coercive Force in Grown Magnetite Crystals from 0.1 μm to 6 mm. *Physics of the Earth and Planetary Interiors* 93: 239–256. https://doi.org/10.1016/0031-9201(95)03071-9.

Hildebrand, A., Penfield, G., Kring, D., Mark, P., Camarago, A., Jacobsen, S., and Boynton, W. 1991. Chicxulub Crater: A Possible Cretaceous/Tertiary Boundary Impact Crater on the Yucatán Peninsula, Mexico. *Geology* 19: 867–871. https://pubs.geoscienceworld.org/gsa/geology/article-abstract/19/9/867/205322/Chicxulub-Crater-A-possible-Cretaceous-Tertiary.

Hode, T., Von Dalwigk, I., and Broman, C. 2004. A Hydrothermal System Associated with the Siljan Impact Structure, Sweden—Implications for the Search for Fossil Life on Mars. *Atrobiology* 3: 271–289. https://doi.org/10.1089/153110703769016370.

Hörz, F., Ostertag, R., and Rainey, D. A. 1983. Bunte Breccia of the Ries: Continuous Deposits of Large Impact Craters. *Reviews of Geophysics* 21: 1667–1725. https://doi.org/10.1029/RG021I008P01667.

Hrouda, F. 2003. Indices for Numerical Characterization of the Alteration Processes of Magnetic Minerals Taking Place during Investigation of Temperature Variation of Magnetic Susceptibility. *Studia Geophysica et Geodaetica* 47: 847–861.

Hüttner, R., Schmidt-Kaler, H., and Treibes, W. 1969. Geologische Übersichts-karte des Ries. *Geologica Bavarica* 61: 451–54.

Iseri, D. A., Geissman, J. W., Newsom, H. E., and Graup, G. 1989. Paleomagnetic and Rock Magnetic Examination of the Natural Remanent Magnetization of Suevite Deposits at Ries Crater, West Germany. *Meteoritics* 24: 280.

Ishihara, S. 1979. Lateral Variation of Magnetic Susceptibility of the Japanese Granitoids. *The Journal of the Geological Society of Japan* 85: 509–523. https://doi.org/10.5575/geosoc.85.509.

Ishihara, S., Hashimoto, M., and Machida, M. 2000. Magnetite/Ilmenite–Series Classification and Magnetic Susceptibility of the Mesozoic-Cenozoic Batholiths in Peru. *Resource Geology* 50: 123–29. https://doi.org/10.1111/J.1751-3928.2000.TB00062.X.

Jackson, M., Borradaile, G., Hudleston, P., and Banerjee, S. 1993. Experimental Deformation of Synthetic Magnetite-

Bearing Calcite Sandstones: Effects on Remanence, Bulk Magnetic Properties, and Magnetic Anisotropy. *Journal of Geophysical Research: Solid Earth* 98: 383–401. https://doi.org/10.1029/92JB01028.

Jackson, M., and Bowles, J. A. 2014. Curie Temperatures of Titanomagnetite in Ignimbrites: Effects of Emplacement Temperatures, Cooling Rates, Exsolution, and Cation Ordering. *Geochemistry, Geophysics, Geosystems* 15: 4343–68. https://doi.org/10.1002/2014GC005527.

Jankowski, B. 1977. Die gradierte Einheit oberhalb des Suevits der Forschungsbohrung Nördlingen 1973.

Just, J., and Kontny, A. 2011. Thermally Induced Alterations of Minerals during Measurements of the Temperature Dependence of Magnetic Susceptibility: A Case Study from the Hydrothermally Altered Soultz-Sous-Forêts Granite, France. *International Journal of Earth Sciences* 101: 819–839. https://doi.org/10.1007/S00531-011-0668-9.

Kletetschka, G., Connerney, J. E. P., Ness, N. F., and Acuña, M. H. 2004. Pressure Effects on Martian Crustal Magnetization near Large Impact Basins. *Meteoritics & Planetary Science* 39: 1839–48. https://doi.org/10.1111/j.1945-5100.2004.tb00079.x.

Kontny, A., Reznik, B., Boubnov, A., Göttlicher, J., and Steininger, R. 2018. Postshock Thermally Induced Transformations in Experimentally Shocked Magnetite. *Geochemistry, Geophysics, Geosystems* 19: 921–931. https://doi.org/10.1002/2017GC007331.

Kring, D. A., Tikoo, S. M., Schmieder, M., Riller, U., Rebolledo-Vieyra, M., Simpson, S. L., Osinski, G. R., et al. 2020. Probing the Hydrothermal System of the Chicxulub Impact Crater. *Science Advances* 6: 3053–82. https://doi.org/10.1126/SCIADV.AAZ3053/SUPPL_FILE/AAZ3053_SM.PDF.

Kruiver, P. P., Dekkers, M. J., and Heslop, D. 2001. Quantification of Magnetic Coercivity Components by the Analysis of Acquisition Curves of Isothermal Remanent Magnetisation. *Earth and Planetary Science Letters* 189: 269–276. https://doi.org/10.1016/S0012-821X(01)00367-3.

Kumar, S., Agarwal, A., Rae, A. S. P., Kontny, A., and Poelchau, M. H. 2023. Use of Magnetic Fabrics and X-ray Diffraction to Reveal Low Strains in Experimentally Deformed Maggia Gneiss. *International Journal of Earth Sciences* 112(3): 867–879. https://doi.org/10.1007/s00531-022-02284-0.

Lattard, D., Engelmann, R., Kontny, A., and Sauerzapf, U. 2006. Curie Temperatures of Synthetic Titanomagnetites in the Fe-Ti-O System: Effects of Composition, Crystal Chemistry, and Thermomagnetic Methods. *Journal of Geophysical Research* 111: 12–28. https://doi.org/10.1029/2006JB004591.

Lied, P., Kontny, A., Nowaczyk, N., Mrlina, J., and Kämpf, H. 2020. Cooling Rates of Pyroclastic Deposits Inferred from Mineral Magnetic Investigations: A Case Study from the Pleistocene Mýtina Maar (Czech Republic). *International Journal of Earth Sciences* 109: 1707–25. https://doi.org/10.1007/S00531-020-01865-1/FIGURES/10.

Lindquist, A. K., Feinberg, J. M., Harrison, R. J., Loudon, J. C., and Newell, A. J. 2015. Domain Wall Pinning and Dislocations: Investigating Magnetite Deformed under Conditions Analogous to Nature Using Transmission Electron Microscopy. *Journal of Geophysical Research: Solid Earth* 120: 1415–30. https://doi.org/10.1002/2014JB011335.

Louzada, K. L., Stewart, S. T., and Weiss, B. P. 2007. Effect of Shock on the Magnetic Properties of Pyrrhotite, the Martian Crust, and Meteorites. *Geophysical Research Letters* 34: 5204. https://doi.org/10.1029/2006GL027685.

Louzada, K. L., Stewart, S. T., Weiss, B. P., Gattacceca, J., Lillis, R. J., and Halekas, J. S. 2011. Impact Demagnetization of the Martian Crust: Current Knowledge and Future Directions. *Earth and Planetary Science Letters* 305: 257–269. https://doi.org/10.1016/j.epsl.2011.03.013.

Mendes, B. D. L., and Kontny, A. 2024. Restoration and Transformation: The Response of Shocked and Oxidized Magnetite to Temperature. *Journal of Geophysical Research* 129(2). https://doi.org/10.1029/2023JB027244.

Mendes, B. D. L., Kontny, A., Poelchau, M., Fischer, L. A., Gaus, K., Dudzisz, K., et al. 2024. Peak-Ring Magnetism: Rock and Mineral Magnetic Properties of the Chicxulub Impact Crater. *Bulletin* 136(1-2): 307–328. https://doi.org/10.1130/B36547.1.

Meyer, C. Sedimentological, Structural and Geochemical Investigations of the Suevite of the Impact Crater Nördlinger Ries, Germany PhD dissertation, Freie Universität Berlin, 2012.

Morrison, R. H., and Oberbeck, V. R. 1978. A composition and thickness model for lunar impact crater and basin deposits. In: Lunar and Planetary Science Conference, 9th, Houston, Tex., March 13-17, 1978, Proceedings. Volume 3. New York, Pergamon Press, Inc., p. 3763–3785.

Muttik, N., Kirsimäe, K., Newsom, H. E., and Williams, L. B. 2011. Boron Isotope Composition of Secondary Smectite in Suevites at the Ries Crater, Germany: Boron Fractionation in Weathering and Hydrothermal Processes. *Earth and Planetary Science Letters* 310: 244–251. https://doi.org/10.1016/J.EPSL.2011.08.028.

Nagy, L., Williams, W., Tauxe, L., and Muxworthy, A. R. 2019. From Nano to Micro: Evolution of Magnetic Domain Structures in Multidomain Magnetite. *Geochemistry, Geophysics, Geosystems* 20: 2907–18. https://doi.org/10.1029/2019GC008319.

Naumov, M. V. 2005. Principal Features of Impact-Generated Hydrothermal Circulation Systems: Mineralogical and Geochemical Evidence. *Geofluids* 5: 165–184. https://doi.org/10.1111/J.1468-8123.2005.00092.X.

Newsom, H. E. 1980. Hydrothermal Alteration of Impact Melt Sheets with Implications for Mars. *Icarus* 44: 207–216. https://doi.org/10.1016/0019-1035(80)90066-4.

Newsom, H. E., Graup, G., Sewards, T., and Keil, K. 1986. Fluidization and Hydrothermal Alteration of the Suevite Deposit at the Ries Crater, West Germany, and Implications for Mars. *Journal of Geophysical Research: Solid Earth* 91: E239–E251. https://doi.org/10.1029/JB091IB13P0E239.

Nishitani, T., and Kono, M. 1981. Grain Size Effect on the Low-Temperature Oxidation of Titanomagnetite. *Journal of Geophysics* 50: 137–142. https://journal.geophysicsjournal.com/JofG/article/view/266.

Oberbeck, V. R. 1975. The Role of Ballistic Erosion and Sedimentation in Lunar Stratigraphy. *Reviews of Geophysics* 13: 337–362. https://doi.org/10.1029/RG013I002P00337.

O'Reilly, W. 1984. Magnetic Properties of Titanomagnetites and Titanomaghemites. In *Rock and Mineral Magnetism*, 132–171. New York, NY: Springer New York. https://doi.org/10.1007/978-1-4684-8468-7_7.

Osinski, G. R. 2005. Hydrothermal Activity Associated with the Ries Impact Event, Germany. *Geofluids* 5: 202–220. https://doi.org/10.1111/j.1468-8123.2005.00119.x.

Osinski, G. R., Grieve, R. A. F., Collins, G. S., Marion, C., and Sylvester, P. 2008. The Effect of Target Lithology on the Products of Impact Melting. *Meteoritics & Planetary Science* 43: 1939–54. https://doi.org/10.1111/J.1945-5100.2008.TB00654.X.

Osinski, G. R. 2003. Impact Glasses in Fallout Suevites from the Ries Impact Structure, Germany: An Analytical SEM Study. *Meteoritics & Planetary Science* 38: 1641–67. https://doi.org/10.1111/J.1945-5100.2003.TB00006.X.

Osinski, G. R. 2004. Impact Melt Rocks from the Ries Structure, Germany: An Origin as Impact Melt Flows? *Earth and Planetary Science Letters* 226: 529–543. https://doi.org/10.1016/J.EPSL.2004.08.012.

Osinski, G. R., Grieve, R. A. F., and Spray, J. G. 2004. The Nature of the Groundmass of Surficial Suevite from the Ries Impact Structure, Germany, and Constraints on its Origin. *Meteoritics & Planetary Science* 39: 1655–83. https://doi.org/10.1111/j.1945-5100.2004.tb00065.x.

Osinski, G. R., Tornabene, L. L., Banerjee, N. R., Cockell, C. S., Flemming, R., Izawa, M. R. M., McCutcheon, J., et al. 2013. Impact-Generated Hydrothermal Systems on Earth and Mars. *Icarus* 224: 347–363. https://doi.org/10.1016/j.icarus.2012.08.030.

Özdemir, Ö., and Dunlop, D. J. 2010. Hallmarks of Maghemitization in Low-Temperature Remanence Cycling of Partially Oxidized Magnetite Nanoparticles. *Journal of Geophysical Research: Solid Earth* 115: 2101. https://doi.org/10.1029/2009JB006756.

Pearce, G. W., and Karson, J. A. 1981. On Pressure Demagnetization. *Geophysical Research Letters* 8: 725–28. https://doi.org/10.1029/GL008I007P00725.

Penfield, G. T., and Camargo, A. Definition of a Major Igneous Zone in the Central Yucatan Platform with Aeromagnetics and Gravity Society of Exploration Geophysicists. Annual Meeting, Tech. Progr, 1981.

Phukon, P., Agarwal, A., Mendes, B. D. L., Kontny, A., and Joshi, G. 2024. Changes in Thermomagnetic and X-ray Diffraction Properties of Asby Dolerite with Distance from the Lockne Impact Structure, Sweden. *Physics of the Earth and Planetary Interiors* 348: 107145. https://doi.org/10.1016/j.pepi.2024.107145.

Pilkington, M., and Grieve, R. A. F. 1992. The Geophysical Signature of Terrestrial Impact Craters. *Reviews of Geophysics* 30: 161–181. https://doi.org/10.1029/92RG00192.

Pohl, J. 1965. Die Magnetisierung der Suevite des Rieses. *Neues Jahrbuch für Mineralogie – Monatshefte* 9: 268–276.

Pohl, J. 1977. Paläomagnetische und gesteinsmagnetische Untersuchungen an den Kernen der Forschungsbohrung Nördlingen 1973. *Geologica Bavarica* 75: 329–348.

Pohl, J., and Angenheister, G. 1969. Anomalien des erdmagnetfeldes und magnetisierung der gesteine im Nördlinger Ries. *Geologica Bavarica* 61: 327–336.

Pohl, J., Klaus Poschlod, W., Reimold, U., Meyer, C., and Jacob, J. 2010. Ries Crater, Germany: The Enkingen Magnetic Anomaly and Associated Drill Core SUBO 18. *Special Paper of the Geological Society of America* 465: 141–163. https://doi.org/10.1130/2010.2465(10).

Pohl, J., Stöffler, D., Gall, H., and Ernstson, K. 1977, 1977. The Ries Impact Crater. In *Impact and Explosion Cratering: Planetary and Terrestrial Implications; Proceedings of the Symposium on Planetary Cratering Mechanics, Flagstaff, Ariz., 1976*, edited by D. J. Roddy, R. O. Pepin, and R. B. Merrill, 343–404. New York: Pergamon Press, Inc.

Rebolledo-Vieyra, M., Urrutia-Fucugauchi, J., and López-Loera, H. 2010. Aeromagnetic Anomalies and Structural Model of the Chicxulub Multiring Impact Crater, Yucatan, Mexico. *Revista Mexicana de Ciencias Geológicas* 27: 185–195. http://www.scielo.org.mx/scielo.php?pid=S1026-87742010000100016&script=sci_arttext&tlng=en.

Reznik, B., Kontny, A., Fritz, J., and Gerhards, U. 2016. Shock-Induced Deformation Phenomena in Magnetite and their Consequences on Magnetic Properties. *Geochemistry, Geophysics, Geosystems* 17: 2374–93. https://doi.org/10.1002/2016GC006338.

Roberts, A. P., Tauxe, L., Heslop, D., Zhao, X., and Jiang, Z. 2018. A Critical Appraisal of the "Day" Diagram. *Journal of Geophysical Research: Solid Earth* 123: 2618–44. https://doi.org/10.1002/2017JB015247.

Sapers, H. M., Osinski, G. R., Flemming, R. L., Buitenhuis, E., Banerjee, N. R., Tornabene, L. L., Blain, S., and Hainge, J. 2017. Evidence for a Spatially Extensive Hydrothermal System at the Ries Impact Structure, Germany. *Meteoritics & Planetary Science* 52: 351–371. https://doi.org/10.1111/maps.12796.

Sato, M., Kurosawa, K., Kato, S., Ushioda, M., and Hasegawa, S. 2021. Shock Remanent Magnetization Intensity and Stability Distributions of Single-Domain Titanomagnetite-Bearing Basalt Sample under the Pressure Range of 0.1–10 GPa. *Geophysical Research Letters* 48: e2021GL092716. https://doi.org/10.1029/2021GL092716.

Sauer, A. 1920. Erläuterungen zur geologischen. Karte Württemberg 1:50,000 Blatt 20 Bopfingen, 15 p.

Schmieder, M., Kennedy, T., Jourdan, F., Buchner, E., and Reimold, W. U. 2018. A High-Precision $^{40}Ar/^{39}Ar$ Age for the Nördlinger Ries Impact Crater, Germany, and Implications for the Accurate Dating of Terrestrial Impact Events. *Geochimica et Cosmochimica Acta* 220: 146–157. https://doi.org/10.1016/J.GCA.2017.09.036.

Schulte, P., Alegret, L., Arenillas, I., Arz, J. A., Barton, P. J., Bown, P. R., Bralower, T. J., et al. 2010. The Chicxulub Asteroid Impact and Mass Extinction at the Cretaceous-Paleogene Boundary. *Science* 327: 1214–18. https://doi.org/10.1126/SCIENCE.1177265/SUPPL_FILE/SCHULTE.SOM.PDF.

Sprain, C. J., Renne, P. R., Clemens, W. A., and Wilson, G. P. 2018. Calibration of Chron C29r: New High-Precision Geochronologic and Paleomagnetic Constraints from the Hell Creek Region, Montana. *GSA Bulletin* 130: 1615–44. https://doi.org/10.1130/B31890.1.

Srnka, L. J., Martelli, G., Newton, G., Cisowski, S. M., Fuller, M. D., and Schaal, R. B. 1979. Magnetic Field and Shock Effects and Remanent Magnetization in a Hypervelocity Impact Experiment. *Earth and Planetary Science Letters* 42: 127–137. https://doi.org/10.1016/0012-821X(79)90198-5.

Stöffler, D. 1977. Research Drilling Nördlingen 1973: Polymict Breccias, Crater Basement, and Cratering Model of the Ries Impact Structure. *Geologica Bavarica* 75: 443–458.

Stöffler, D., and Grieve, R. A. F. 2007. Impactites. In *Metamorphic rocks: A Classification and Glossary of Terms, Recommendations of the International Union of Geological Sciences*, 82–92. Cambridge: Cambridge University Press.

Tarling, D. H., and Hrouda, F. 1993. *The Magnetic Anisotropy of Rocks*. Berlin/Heidelberg: Springer Science & Business Media. https://link.springer.com/book/9780412498800.

Tikoo, S., Zylberman, W., Quesnel, Y., Gattacceca, J., Rebolledo-Vieyra, M., and Fucugauchi, J. U. 2017. Paleomagnetic insights into impact-related hydrothermal systems and magnetic anomalies at the Chicxulub crater. In *AGU Fall Meeting Abstracts*, vol. 2017, P23H-05.

Tikoo, S. M., Gattacceca, J., Swanson-Hysell, N. L., Weiss, B. P., Suavet, C., and Cournède, C. 2015. Preservation and Detectability of Shock-Induced Magnetization. *Journal of Geophysical Research: Planets* 120: 1461–75. https://doi.org/10.1002/2015JE004840.

Ugalde, H., Artemieva, N., and Milkeriet, B. 2005. Magnetization on Impact Structures—Constraints from Numerical Modeling and Petrophysics. In *Large Large meteorite Impacts*, vol. III, 25–42. Boulder, CO: Geological Society of America.

Urrutia-Fucugauchi, J., Camargo-Zanoguera, A., Mexicanos, P., Urrutia-Fucugauchi, J., Camargo-Zanoguera, A., Pérez-Cruz, L., Pérez-Cruz, G., Pérez-Cruz, L., and Pérez-Cruz, G. 2011. The Chicxulub Multi-Ring Impact Crater, Yucatan Carbonate Platform, Gulf of Mexico. *Geofisica Internacional* 50(1): 99–127.

Verwey, E. J. W. 1939. Electronic Conduction of Magnetite (Fe_3O_4) and its Transition Point at Low Temperatures. *Nature* 144: 327–28. https://doi.org/10.1038/144327b0.

Wünnemann, K., Collins, G. S., and Osinski, G. R. 2008. Numerical Modelling of Impact Melt Production in Porous Rocks. *Earth and Planetary Science Letters* 269: 530–39. https://doi.org/10.1016/J.EPSL.2008.03.007.

Zhao, Z., Zieger, L., Littke, R., and Schwarzbauer, J. 2022. Structural and Chemical Variability and Provenance of Lacustrine Organic Matter in the Miocene Nördlinger Ries Post-Impact Sediments. *International Journal of Coal Geology* 262: 104112. https://doi.org/10.1016/j.coal.2022.104112.

SUPPORTING INFORMATION

Additional supporting information may be found in the online version of this article.

File S1. Ries magnetic mineralogy: Exploring impact and post-impact evolution of crater magnetism.